Electrically tunable optical active metasurfaces in space and time

Thesis by
Jared Sisler

In Partial Fulfillment of the Requirements for the
Degree of
Doctor of Philosophy

CALIFORNIA INSTITUTE OF TECHNOLOGY
Pasadena, California

2026
Defended November 20, 2025

Jared Sisler
ORCID: 0000-0002-0660-7909

ACKNOWLEDGEMENTS

The completion of my thesis was made possible by the support (academically and personally) of many people in the Caltech community and beyond. Here, I will do my best to recognize those who helped me along my PhD journey.

First and foremost, I would like to thank my advisor, Professor Harry Atwater, for his unwavering support throughout my time at Caltech. His optimism, patience, and scientific curiosity gave me a unique opportunity to explore difficult problems without being limited by lab resources or timelines. I am very grateful for the trust he placed in me from the beginning of my PhD and for making the Atwater Group an enjoyable place to be.

I am also grateful to my committee, Professors Andrei Faraon, Axel Scherer, and Kerry Vahala, for their support and valuable feedback throughout my PhD. In particular, I would like to thank Professor Faraon for chairing both my PhD candidacy and defense sessions and for co-supervising one of my research projects. I greatly enjoyed our collaboration and I appreciate his advice and support throughout my PhD.

During my time at Caltech, I had the opportunity to collaborate with many other brilliant researchers. Thank you to Professor Claudio Hail for his generous time assisting and mentoring me in the lab as well as for being a great friend. He was always my go-to person for questions about nanofab, optical setups, or simulations and I am grateful for his patience and support at all times. Thank you also to Dr. Prachi Thureja, with whom I worked closely during the first few years of my PhD, for all your research contributions and for helping me get started in the lab. Additionally, thank you to Dr. Meir Grajower for your patience and mentoring, especially related to all things experiment and measurement. Thank you to Dr. Ruzan Sokhoyan for being a great office-mate and for sharing your knowledge and perspective on active metasurfaces. Thank you to Dr. Michael Kelzenberg for your time building and debugging the electronics that enabled many exciting measurements of our active metasurface devices. Thank you also to Dr. Komron Shayegan for all the great research discussions related to thermal photonics and everyone's favorite material, ITO. Thank you to Phillippe Pearson for being a great collaborator and for making our project so enjoyable. I am very grateful for all the fabrication and materials-related advice Dr. Phil Jahelka has provided throughout my time in the Atwater

Group. His constant willingness to help or just discuss an interesting topic was invaluable to me as well as the entire Atwater Group. I would also like to thank John Hylak, Dr. Ramon Gao, Dr. Lior Michaeli, Dr. Souvik Biswas, for their friendship and support. In addition, all members of the Atwater Group made my PhD very enjoyable.

I also had the amazing opportunity to collaborate with many excellent researchers at the company, Seurat Technologies, throughout my PhD. I thoroughly enjoyed our collaboration and their contribution to our project was invaluable. Thank you to Dr. Selim Elhadj for his vision and guidance. Thank you to Dr. Zoey Davidson for his contributions, especially from his vast knowledge of liquid crystals, which was a critical contributor to the success of our project. Additionally, I would like to thank Dr. Jiannan Gao and Dr. Austin Fehr for their efforts in creating reliable devices and taking high-power measurements.

Another exciting collaboration during my PhD took place with members of the optical communication team at the Jet Propulsion Laboratory (JPL). Thank you to Dr. Abhijit Biswas, Dr. Joseph Kovalik, Dr. William Roberts for their support and mentorship during my time spent at JPL. Additionally, I would like to thank Vachik Garkanian, Carlos Esproles, and Malcolm Wright for their contributions to our project.

The majority of my time at Caltech was spent working two floors underground in the Kavli Nanoscience Institute (KNI) and I would like to thank the entire KNI staff for their time keeping tools operational. Thank you to Dr. Guy A. DeRose, Alex Wertheim, Bert Mendoza, Dr. Annalena Wolff, Dr. Alireza Ghaffari, Kelly McKenzie, Nathan Lee, Tiffany Kimoto, Jennifer Palmer, and Syndney Garstang. Thank you especially to Alex and Bert for spending extra time to share their knowledge of vacuum systems, materials science, and nanofabrication which was invaluable throughout my PhD.

I would also like to thank all the Caltech administrative staff for keeping things running and for their support. In particular, I really appreciated the efforts of Thomasine Murphy, Jennifer Blankenship, Christy Jenstad, and Kam Flower for their behind-the-scenes work to keep research going in the Atwater Group.

During my undergraduate degree, I had the amazing opportunity to spend time in many different research groups. These experiences shaped my interest in pursuing a career in academia and taught me a lot about how to conduct research. First of all, I

would like to thank Professors Michael Tam, Steven Bryant, Federico Capasso, and Ted Sargent for supporting me in their labs and giving me the opportunity to take part in research when I was an undergraduate student. In particular, I would like to thank Dr. Wei-Ting Chen with whom I worked very closely for eight months in the group of Prof. Capasso. Wei-Ting was, by far, the most generous person I have ever worked with and he spent countless hours teaching me about metasurface design, simulation, measurements, and research in general. I learned a tremendous amount from his mentorship and I am extremely grateful for all of his help. Additionally, I would like to thank Prof. Noah Rubin, Dr. Tyler Stephenson, and Dr. Shimin Shi for their mentorship and support.

In addition to those with whom I directly collaborated, there are many others who have allowed me to be successful at Caltech by making my time outside the lab so enjoyable. First and foremost, thank you to Dan and Phil for being my go-to study partners, research advisors, and riff-mates for the past decade. Their attention to detail, work ethic, and sense of humour allowed me to work long hours through my undergrad and PhD and still have fun while doing it. Without them, I certainly would not have made it this far — or remained this sane. Additionally, thank you to Ben and Charles for being amazing friends and making my time in Pasadena so enjoyable. Looking back, I think the years when all five of us were at Caltech will obtain the "Golden Years" classification. Thank you, also, to Komron, Ryoto, and Nico who were great friends on and off the bike.

And finally, thank you to Mom, Dad, and Kealan for your constant support while I was away from home.

ABSTRACT

Controlling the properties of light in space and time is fundamental to many areas of science and engineering. In recent years, actively tunable metasurfaces have enabled dynamic and precise manipulation of the wavefront of light in a compact form-factor, paving the way for a revolution in optics and photonics. This thesis furthers our understanding of such active nanophotonic devices and experimentally presents advanced control over light using two distinct material platforms: indium tin oxide (ITO) and liquid crystals (LCs). The conclusions from this work will enable the design and fabrication of more sophisticated active optical devices.

We start with an introduction to metasurfaces by providing a brief history of their development and the physics of their operation. We then outline the subfield of active metasurfaces and provide the relevant background for the remainder of this thesis.

Chapter 2 continues with a detailed background on ITO by summarizing its properties, common deposition methods, and methods of characterization. We then provide an in-depth analysis of how the properties of ITO can be changed through annealing in different material environments. This underpins much of the work that is presented in Chapters 3–5 of this thesis.

Using the principles introduced in Chapter 2, we present a method to create precisely defined lateral doping gradients in a thin film of ITO. Our process selectively dopes regions of ITO via patterning a low-quality oxide layer on top of a planar film of ITO, followed by a low temperature (150 °C) anneal and the removal of the evaporated Al_2O_3. We fabricate reflective gratings of varying periodicity and demonstrate plasmonic guided modes in an unpatterned film of ITO. This work paves the way for ITO films to be integrated in more complex photonic devices such as on-chip modulators and free-space metasurfaces, as well as furthering our understanding of the material and optical properties of ITO.

Next, we demonstrate an ITO-based electrically tunable reflective metasurface in the midwave-infrared (mid-IR). This device operates by electrically modulating the carrier concentration in ITO when placed in a gap plasmon resonator to control the phase and amplitude of scattered light across a surface. Through appropriate electrical and optical design, we demonstrate the polarization-independent tunable diffraction of light in two dimensions (2D). This device represents a significant step

forward for solid-state beam-steering devices in the mid-IR which are essential to applications such as thermal imaging and gas sensing.

In Chapter 5, we experimentally show the electrical spatiotemporal modulation of an ITO-based metasurface in the near-infrared (near-IR) for the generation and tunable diffraction of high frequency signals. In this work, we use a similar device design as was used to demonstrate mid-IR beam-steering. We first modulate our device with frequencies up to 10 MHz to generate sidebands offset from the near-IR incident laser frequency. Through temporal waveform engineering, we generate select sidebands of interest and suppress unwanted sidebands. Finally, by spatially varying the time-delay of the temporal modulation, we can diffract — or normally reflect — each generated frequency. This device paves the way towards active metasurfaces for multi-beam, multi-frequency functionalities such as free-space optical communication.

Finally, we present a highly transmissive active metasurface enabling polarization rotation of near-IR light in 2D using a LC infiltrated titanium dioxide (TiO_2) metasurface. Our device consists of a subwavelength periodic array of TiO_2 nanopillars submerged in a thin (2 μm) LC layer and supports electric and magnetic dipole modes. Using a biased photoactive top contact, we spatially control the polarization rotation of transmitted light in 2D through the patterning of a 435 nm pump laser on the surface of the device. This work represents a significant contribution to LC-based optical devices through the detailed modeling of LC interactions with TiO_2 nanostructures to enable the efficient modulation of a large-area active metasurface.

This thesis presents many aspects of materials fabrication, characterization, and modeling which are fundamental to the development of the next generation of active photonic devices.

PUBLISHED CONTENT AND CONTRIBUTIONS

[1] **J. Sisler**[†], P. Thureja[†], M. Y. Grajower, R. Sokhoyan, I. Huang, and H. A. Atwater, "Electrically tunable space–time metasurfaces at optical frequencies," *Nature Nanotechnology*, vol. 19, pp. 1491–1498, 10 2024. DOI: 10.1038/s41565-024-01728-9,
[†] These authors contributed equally to this work

J.S. co-conceived of the ideas for this research project, fabricated and characterizated the metasurfaces, built the experimental setup for space-time modulation, performed quasi-static and time-modulated measurements, performed the space-time measurements, created the real-time waveform optimization algorithm, performed the space-time calculations, and wrote the manuscript.

[2] **J. Sisler**, P. Pearson, M. Kelzenberg, A. Faraon, and H. A. Atwater, "Electro-optic modulation of coherent and incoherent mid-IR radiation in two-dimensional arrays," 2026. arXiv: 2603.02401 [physics.optics]. [Online]. Available: https://arxiv.org/abs/2603.02401,

J.S. fabricated the active metasurfaces, assisted in device measurements, and co-wrote the manuscript.

[3] **J. Sisler**, C. U. Hail, Z. S. Davidson, J. Gao, A. Fehr, R. Sokhoyan, S. Elhadj, and H. A. Atwater, "An optically addressable transmissive liquid crystal metasurface spatial light modulator," 2026. arXiv: 2603.20574 [physics.optics]. [Online]. Available: https://arxiv.org/abs/2603.20574,

J.S. fabricated and characterized the TiO_2 metasurfaces, performed all optical measurements, performed all multiphysics simulations, and wrote the manuscript.

[4] **J. Sisler**, K. Shayegan, and H. A. Atwater, "Planar gratings enabled by spatially controlled doping of ITO thin films," 2026. *In Preparation*,

J.S. developed the fabrication process, fabricated all devices, performed optical measurements and simulations, and co-wrote the manuscript.

[5] R. Sokhoyan, P. Thureja, **J. Sisler**, M. Y. Grajower, K. Shayegan, E. Feigenbaum, S. Elhadj, and H. A. Atwater, "Electrically tunable conducting oxide metasurfaces for high power applications," *Nanophotonics*, vol. 12, pp. 239–

253, 2 2023. DOI: 10.1515/nanoph-2022-0594,

J.S. fabricated the metasurfaces and performed high-power measurements.

[6] P. Thureja, R. Sokhoyan, C. U. Hail, **J. Sisler**, M. Foley, M. Y. Grajower, and H. A. Atwater, "Toward a universal metasurface for optical imaging, communication, and computation," *Nanophotonics*, vol. 11, pp. 3745–3768, 17 2022. DOI: 10.1515/nanoph-2022-0155,

J.S. co-conceived the ideas presented in this perspective, created many of the figures, and wrote a section of the main text.

TABLE OF CONTENTS

LIST OF ILLUSTRATIONS

LIST OF TABLES

Chapter 1

INTRODUCTION

1.1 Metasurfaces: Engineering the wavefront of light

Metasurfaces are two-dimensional (2D) arrays of subwavelength scatterers that can shape the phase, amplitude, and polarization of an output wavefront of light. They are descendants of metamaterials: three-dimensional (3D) structures consisting of periodic subwavelength resonant meta-atoms. The design and experimental realization of radiofrequency (RF) metamaterials was an active area of research in the 2000s. During this time, researchers sought to create an "artificial medium" with exotic electromagnetic properties, such as negative refractive index, not yet observed in naturally occurring materials. Theoretical predictions of exciting phenomena such as the "perfect lens" breaking the diffraction limit [1] and invisibility [2] drove significant interest in the field. Despite interest in the optics community, high loss and strong dispersion in the meta-atom units limited the experimental realization of previously proposed effects. Additionally, the fabrication of 3D structures proved difficult, especially for devices operating at shorter wavelengths. Thus, metasurfaces — effectively the 2D counterpart of metamaterials — became a more attainable goal for the field. While the underlying concepts of metasurfaces had existed in antenna theory and diffractive optics for decades [3], a 2011 work by Yu et al. [4] framed these ideas in a more modern perspective and sparked significant interest in the optics community.

The electromagnetic response of metamaterials is governed by the propagation of light over multiple wavelengths. Instead of relying on the polarizability of naturally occurring materials, the substituent meta-atoms, with judiciously designed resonances, created an effective medium through which light propagates. Metasurfaces, however, shape light in a fundamentally different way. Due to their subwavelength thickness, metasurfaces can not rely on the propagation of light and, thus, are typically designed around resonances of each sub-atom to create a subwavelength discontinuity to the propagation of light. Yu et al. [4] described this effect by revisiting Fresnel's laws of reflection and reflection for the case where a phase discontinuity can be engineered across a subwavelength surface. They described a "Generalized Snell's Law" which explicitly included the lateral phase gradient

imparted by the metasurface to the scattered angle of light. For a transmitted beam, this results in

$$sin(\theta_t)n_t - sin(\theta_i)n_i = \frac{\lambda_0}{2\pi}\frac{d\Phi}{dx} \tag{1.1}$$

where n_i and θ_i are the refractive index and angle of incidence of light, respectively, n_t and θ_t are the refractive index and angle of refracted light, respectively, λ_0 is the free-space wavelength of light, and $\frac{d\Phi}{dx}$ is the lateral phase gradient imparted by the surface. It follows from equation (1.1) that the spatial phase gradient of the metasurface imparts lateral momentum to the outgoing light. This result is schematically depicted in Fig. 1.1.

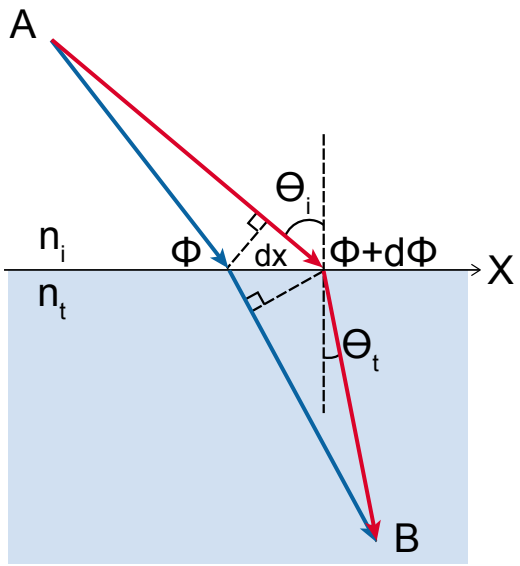

Figure 1.1: Generalized Snell's law. Figure redrawn from [4].

Using plasmonic antennas designed at $\lambda = 8\ \mu$m, Yu et al. [4] also provided an intuitive design approach to achieve full 2π phase coverage with high efficiency and a simple fabrication process. This seminal work inspired an explosion of metasurface research which continues to this day.

Now that the fundamental principles of metasurfaces have been introduced, the following sections will highlight some important developments in metasurface research over the past ~15 years.

Passive metasurfaces

Passive metasurfaces have a fixed optical response in time. They represent the majority of metasurface research and have experimentally realized a diverse range of optical phenomena such as beam deflection [5, 6], focusing [7, 8, 9, 10], polariza-

tion conversion [11, 12, 13], and holography [14, 15]. Many passive metasurfaces replicate the functionality of conventional optics elements such as lenses, polarizers, and filters in a more compact and lightweight form-factor. In the mid-2010s, there was significant interest in creating metasurface lenses, referred to as metalenses. It was imagined that metalenses would replace refractive lenses in consumer devices such as smartphone cameras to enable lighter and thinner phones [16]. Progress was made in the development of dispersion engineering techniques for achromatic metalenses [8, 10], but fundamental difficulties associated with achieving large group delay and maintaining performance for a large field of view limited the widespread use of metalenses as a replacement for refractive optics. While metalenses were unable to replace refractive lenses for imaging of visible wavelengths — a technology which has been developed over the course of centuries — they could find use in more specialized imaging applications. Metalenses can excel, for example, when designed for operating wavelengths where refractive lenses are difficult to design, such as the extreme ultraviolet (EUV) [17], or in applications where only a narrow range of wavelengths are required [18]. In general, metasurfaces will make their greatest contribution by enabling new optical functionalities rather than replacing existing conventional optics with a smaller form-factor. A few examples of new functionalities enabled by passive metasurfaces include space compression [19], coherent thermal emission [20], and the shaping of frequency-converted wavefronts [21].

Passive metasurfaces can be broadly grouped into two categories: local and non-local. In local metasurfaces, the interaction of light with each subwavelength scatterer is localized and there is little coupling between adjacent structures. These resonances tend to have low quality (Q)-factors due to short temporal coherence lengths. Mie resonances such as electric and magnetic multipoles are examples of local resonances. In contrast, non-local metasurfaces make use of long-range optical modes that rely on the coupling between many subwavelength elements. These tend to have high Q-factors formed by long temporal coherence lengths. Guided mode resonances (GMRs) are examples of non-local resonances. The majority of metasurface demonstrations have been designed using local resonances because they allow precise spatial control over amplitude, phase, and polarization at each point across the 2D surface for the tailoring of desired output wavefronts.

The design of local metasurfaces is most commonly performed by first building a “library” of meta-atom elements with a known phase and amplitude response

in transmission or reflection. This is typically achieved by simulating structures of fixed height with a range of different in-plane geometries [22]. The meta-atoms can be metallic or dielectric and can support a range of different optical modes, provided their optical modes are mostly confined to their unit cell. Periodic boundary conditions are often assumed during the building of these libraries in order to approximate the response of the meta-atom in the final metasurface. Once a sufficiently large library of elements is constructed, one can place meta-atoms at discretized positions across the 2D surface of the metasurface with the closest phase and amplitude to the design of interest. The general library-based design approach is visually depicted in Fig. 1.2 for the specific case of designing a 1D metalens.

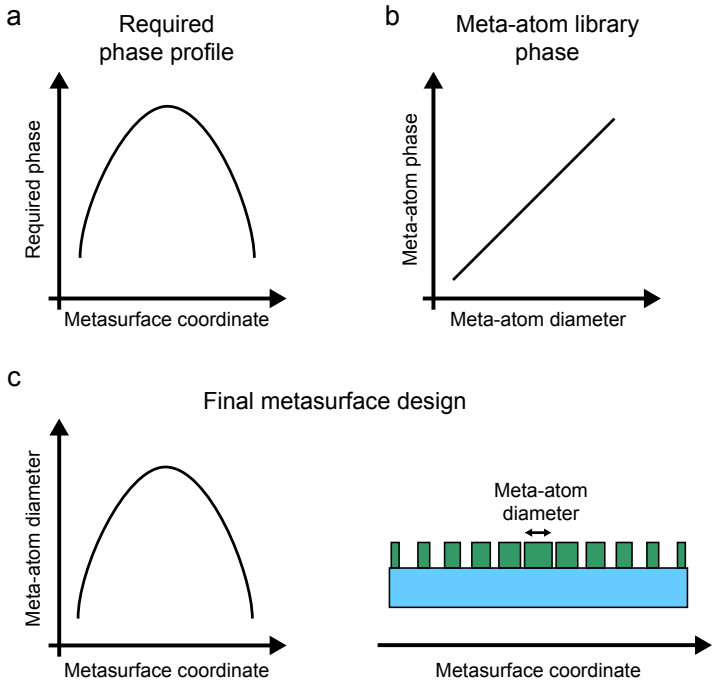

Figure 1.2: Library method of designing a passive metasurface. (a) First, obtain the required phase across the metasurface aperture. Here, the approximate phase profile for a 1D lens is shown. (b) Generate a meta-atom phase library by sweeping some geometrical parameter of design nanostructure. Here, we show the scattered phase as a function of the diameter of cylindrical meta-atom posts. (c) For each coordinate across the device, place the meta-atom with the closest phase to the target phase profile. Left panel shows the meta-atom diameter as a function of metasurface coordinate and the right panel shows the corresponding schematic cross-section of the final metasurface/metalens.

Using the library method, if there is any coupling between adjacent elements, it is generally assumed that the geometric variation of meta-atoms across the surface is gradual enough such that the coupling between adjacent structures does

not significantly change the scattered field from what was calculated during the library-building phase. This assumption does not hold for the design of non-local metasurfaces because the optical response of each individual meta-atom is highly dependent on its neighbour. The design of such metasurfaces cannot use the typical library design method. Typically, non-local metasurfaces are designed through aperture-scale inverse design techniques [23, 24] or by engineering the photonic bands of the metasurface [25, 26].

Active metasurfaces

Active metasurfaces are a subset of metasurfaces that can change their optical response in time as a function of some external stimulus (e.g. applied voltage, local heating, mechanical deformation). They are often designed around a tunable material whose refractive index can be dynamically tuned. However, physically achievable changes in index are often small or occur in small volumes. To enhance the achievable modulation, a periodic subwavelength array of identical resonant meta-atoms are often placed on top of the active medium to increase the interaction of light with the material. Then, by applying some stimulus across the aperture, the functionality of the metasurface can be dynamically tuned. While active metasurfaces can be realized in many different ways, the applied stimulus is often an applied voltage — which is applied to the metasurface with an array of electrical interconnects — and the individual resonators often support local resonances. In this configuration, a library-based design approach can be applied to active metasurfaces, analogous to the method used for the design of passive metasurfaces. Here, the library of phase and/or amplitude is built in a parameterized space of applied voltage rather than meta-atom geometry. Much of the existing literature on active metasurfaces has explored different materials and tuning mechanisms to achieve large and fast optical modulation with high efficiency. Although each of these requirements has been achieved separately, it is difficult to achieve all three in a single material platform.

In Fig. 1.3 we highlight some of the common methods used to realize active metasurfaces and summarize their respective benefits/challenges. This is not an exhaustive list but provides some insight on the field. Mechanical actuation has been primarily implemented in active metasurfaces by using a microelectromechanical system (MEMS) to introduce strain to a soft substrate to change the periodicity of individual meta-atoms or by deforming regions of the metasurface [28, 29, 30]. These systems can achieve large optical modulation and are often efficient, but

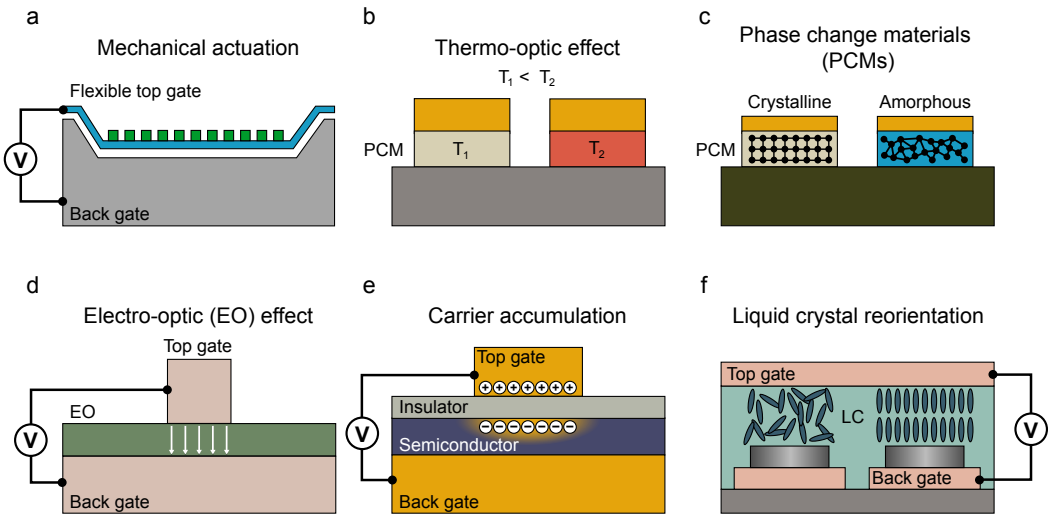

Figure 1.3: Overview of active metasurface modulation techniques. (a) Mechanical actuation: An applied voltage deforms the metasurface aperture. (b) Thermo-optic effect: A change in temperature results in a change in refractive index. (c) Phase change materials (PCMs): A change in crystal structure results in a change in refractive index. (d) Electro-optic (EO) effect: An applied electric field changes the refractive index in a specific crystal axis. (e) Carrier accumulation: An applied electric field accumulates or depletes carriers in a semiconductor-like material. (f) Liquid crystal reorientation: An applied electric field changes orientation of liquid crystals. Figure adapted from [27].

they are limited to slow modulation speeds. Thermo-optic tuning can achieve large optical modulation and can even be designed to modulate at frequencies of 100 kHz [31], but it can be difficult to demonstrate high spatial resolution due to thermal crosstalk between meta-atoms [32, 33]. Phase-change materials (PCMs) can exhibit large optical modulation at moderate speeds (10s kHz), but through the Kramers-Kronig relations, the large change in the real part of the refractive index is accompanied by a large change in the imaginary part, limiting the overall efficiency [34, 35, 36, 37]. Additionally, it can be difficult to continuously tune the optical response using PCMs and they are often used to switch between two predetermined optical functions. Electro-optically tuned metasurfaces using the Pockels or Kerr effect in ferromagnetic dielectrics such as lithium niobate [38, 39] or barium titanate [40] can be modulated at high frequencies (100s of GHz) [41] with very little loss, but the magnitude of optical modulation is limited, which requires the design of high-Q resonators to enhance the optical interaction with the material. Thus, it is difficult to achieve complex spatial functions such as beam-steering in 2D as the high-Q resonators often require an extended mode in

one dimension. Electro-optic modulation using carrier accumulation in transparent conducting oxides (TCOs) such as indium tin oxide (ITO) [42, 43, 44] or Fermi-level modulation in 2D transition metal dichalcogenides (TMDCs) [45] has achieved large phase shift at fast (GHz) speeds [46], but often have low efficiency due to free-carrier absorption. Finally, active metasurfaces actuated using liquid crystal (LC) reorientation has demonstrated large tunability with high efficiency, but is inherently limited to ~kHz speeds due to slow LC relaxation times [47, 48, 49]. The last two modulation mechanisms — gate-tunable carrier accumulation/depletion in ITO and LC reorientation — form the foundation of this thesis and will be discussed in more detail throughout.

An ideal active metasurface would be able to switch between any functionality of a passive metasurface by rearranging the voltages sent to the device. The field of active metasurfaces, however, is currently far from such a "universal" device, and experimental demonstrations to date have focused on realizing a smaller subset of functionalities such as dynamic beam-steering/beam-forming and tunable focusing [44, 50]. One of the main applications of a solid-state beam-steering device (such as an active metasurface) is to replace conventional beam-scanning systems which rely on MEMS-based mirror actuators. While these systems have excellent efficiency and can achieve moderate switching speeds (100s kHz) [51], they are inherently bulky and can have poor reliability because of their moving components. This can make them poor choices for applications — such as beam-pointing in satellites — where reliability, size, and weight are important factors. Active metasurfaces can provide an alternative to conventional beam-pointing devices and adaptive optics for the emerging field of free-space optical communication [52].

Operation Modes of Active Metasurfaces

All active metasurfaces can change their optical response as a function of time. However, the way in which their response is modulated can be grouped into the three regimes shown in Fig. 1.4. In most cases, they are switched between various configurations and kept in their final state at a time-scale much longer than their switching time. This operation mode, depicted in Fig. 1.4a, is referred to as "Quasi-Static" and could be used for a tunable lens in an imaging system. In this case, the metasurface imparts lateral momentum to the outgoing wavefront, but the frequency, f_0, remains the same. In the second modulation regime, depicted in Fig. 1.4b, all meta-atoms are modulated in-time and in-phase with each other. This results in energy being transferred to the outgoing light in the form of frequency

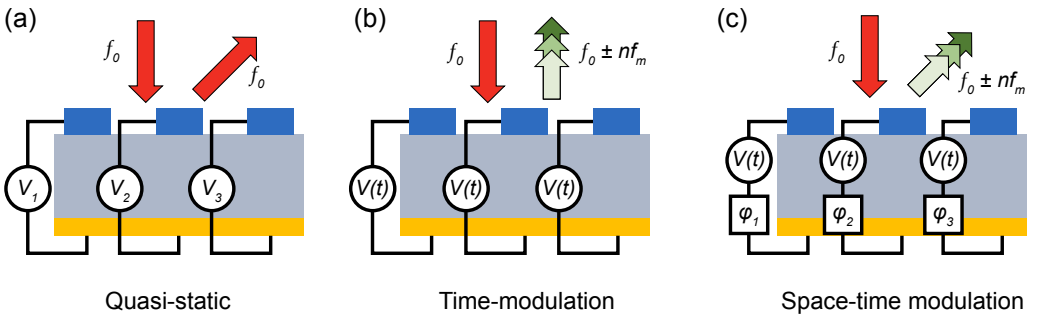

Figure 1.4: Operation modes of an active metasurface. (a) Quasi-static: This changes the momentum of output light, but keeps the frequency the same. (b) Time-modulation: This keeps the momentum of output light the same, but changes the frequency. (c) Space-time modulation: This combines both (a) and (b) to change both the momentum and frequency of output light. Figure from [27].

sidebands, $f_0 \pm nf_m$. However, as there is no spatial phase gradient, the outgoing angle matches that of the incoming light. It should be noted here that experimental observation of these frequency sidebands requires that the modulation frequency, f_m, be greater than the linewidth of the incident light. As common lasers have linewidths on the order of 10s–100s kHz, the observation of this phenomenon does not require significant high-speed driving electronics. Finally, we can combine these two regimes by modulating the entire metasurface with a given temporally varying signal and time-delaying this signal between adjacent meta-atoms. This space-time modulation scheme is depicted in Fig. 1.4c and enables the simultaneous frequency generation and beam deflection in a single device. Throughout this thesis, all three of these modulation regimes will be discussed and experimentally demonstrated.

1.2 Scope of this thesis

This thesis presents novel electrically tunable active metasurface devices operating at optical wavelengths. These devices use two active materials: indium tin oxide (ITO) and liquid crystals (LCs). In addition to presenting final device demonstrations, we provide a detailed description of the many materials challenges that were faced along the way. These challenges proved to be the main limiting factors in the demonstration of an effective and efficient final optical device.

We start by dedicating an entire chapter (Chapter 2) to outline our empirical knowledge gained concerning the material properties of ITO. First, we describe the process we developed for the repeatable fabrication of ITO-based active metasurfaces. Then, we provide a comprehensive description of how ITO interacts with a variety

of different materials.

In Chapters 3–5, we present three novel ITO-based metasurfaces. First, we present a novel process for creating spatially varying doping profiles in thin films of ITO. These passive metasurfaces demonstrate strong plasmonic grating modes in reflection for a planar film of ITO. Next, we show an active beam-steering metasurface capable of the polarization independent tunable diffraction of mid-IR light in 2D. We use this same device to also demonstrate the micron-scale 2D patterning of emissivity. Finally, we use a similar device architecture (this time designed in the near-IR) for the simultaneous generation of near-arbitrary frequency spectra in the MHz and the independent switchable diffraction of each generated frequency.

In Chapter 6, we present an all-optically addressed LC-infiltrated TiO_2 metasurface for the 2D patterning of converted polarization light in the near-IR. Our device achieves faster modulation speeds than equivalently designed devices without a TiO_2 metasurface layer. Additionally, we present a multiphysics approach to model the dynamics of the LCs on a molecular level when in contact with nanostructured TiO_2 structures and in the presence of spatially varying electric fields. This model provides an improved prediction of the final transmitted optical modulation and shows good agreement with measurement.

Finally, in Chapter 7 we provide a summary of our work and highlight the advancements provided within this thesis. We then describe our outlook for the field. For each research project presented, we introduce multiple future directions that could be explored.

References

[1] J. B. Pendry, "Negative refraction makes a perfect lens," *Physical Review Letters*, vol. 85, pp. 3966–3969, 18 2000. DOI: 10.1103/PhysRevLett.85.3966.

[2] D. Schurig, J. J. Mock, B. J. Justice, S. A. Cummer, J. B. Pendry, A. F. Starr, and D. R. Smith, "Metamaterial electromagnetic cloak at microwave frequencies," *Science*, vol. 314, pp. 977–980, 5801 2006. DOI: 10.1126/science.1133628.

[3] P. Lalanne, S. Astilean, P. Chavel, E. Cambril, and H. Launois, "Blazed binary subwavelength gratings with efficiencies larger than those of conventional échelette gratings," *Optics Letters*, vol. 23, p. 1081, 14 1998. DOI: 10.1364/OL.23.001081.

[4] N. Yu, P. Genevet, M. A. Kats, F. Aieta, J.-P. Tetienne, F. Capasso, and Z. Gaburro, "Light propagation with phase discontinuities: Generalized laws of reflection and refraction," *Science*, vol. 334, pp. 333–337, 6054 2011. DOI: 10.1126/science.1210713.

[5] D. Sell, J. Yang, S. Doshay, R. Yang, and J. A. Fan, "Large-angle, multifunctional metagratings based on freeform multimode geometries," *Nano Letters*, vol. 17, pp. 3752–3757, 6 2017. DOI: 10.1021/acs.nanolett.7b01082.

[6] X. Ni, N. K. Emani, A. V. Kildishev, A. Boltasseva, and V. M. Shalaev, "Broadband light bending with plasmonic nanoantennas," *Science*, vol. 335, pp. 427–427, 6067 2012. DOI: 10.1126/science.1214686.

[7] M. Khorasaninejad, W. T. Chen, R. C. Devlin, J. Oh, A. Y. Zhu, and F. Capasso, "Metalenses at visible wavelengths: Diffraction-limited focusing and subwavelength resolution imaging," *Science*, vol. 352, pp. 1190–1194, 6290 2016. DOI: 10.1126/science.aaf6644.

[8] W. T. Chen, A. Y. Zhu, V. Sanjeev, M. Khorasaninejad, Z. Shi, E. Lee, and F. Capasso, "A broadband achromatic metalens for focusing and imaging in the visible," *Nature Nanotechnology*, vol. 13, pp. 220–226, 3 2018. DOI: 10.1038/s41565-017-0034-6.

[9] A. Arbabi, Y. Horie, M. Bagheri, and A. Faraon, "Dielectric metasurfaces for complete control of phase and polarization with subwavelength spatial resolution and high transmission," *Nature Nanotechnology*, vol. 10, pp. 937–943, 11 2015. DOI: 10.1038/nnano.2015.186.

[10] E. Arbabi, A. Arbabi, S. M. Kamali, Y. Horie, and A. Faraon, "Controlling the sign of chromatic dispersion in diffractive optics with dielectric metasurfaces," *Optica*, vol. 4, p. 625, 6 2017. DOI: 10.1364/optica.4.000625.

[11] J. B. Mueller, N. A. Rubin, R. C. Devlin, B. Groever, and F. Capasso, "Metasurface polarization optics: Independent phase control of arbitrary orthogonal

states of polarization," *Physical Review Letters*, vol. 118, p. 113 901, 11 2017. DOI: 10.1103/PhysRevLett.118.113901.

[12] R. C. Devlin, A. Ambrosio, N. A. Rubin, J. P. B. Mueller, and F. Capasso, "Arbitrary spin-to–orbital angular momentum conversion of light," *Science*, vol. 358, pp. 896–901, 6365 2017. DOI: 10.1126/science.aao5392.

[13] N. A. Rubin, G. D'Aversa, P. Chevalier, Z. Shi, W. T. Chen, and F. Capasso, "Matrix fourier optics enables a compact full-stokes polarization camera," *Science*, vol. 364, 6448 2019. DOI: 10.1126/science.aax1839.

[14] X. Ni, A. V. Kildishev, and V. M. Shalaev, "Metasurface holograms for visible light," *Nature Communications*, vol. 4, p. 2807, 1 2013. DOI: 10.1038/ncomms3807.

[15] G. Zheng, H. Mühlenbernd, M. Kenney, G. Li, T. Zentgraf, and S. Zhang, "Metasurface holograms reaching 80% efficiency," *Nature Nanotechnology*, vol. 10, pp. 308–312, 4 2015. DOI: 10.1038/nnano.2015.2.

[16] L. S. R. Letzter, "Metalens breakthrough may bring a revolution in camera design," *NBC News*, Jan. 2018.

[17] M. Ossiander, M. L. Meretska, H. K. Hampel, S. W. D. Lim, N. Knefz, T. Jauk, F. Capasso, and M. Schultze, "Extreme ultraviolet metalens by vacuum guiding," *Science*, vol. 380, pp. 59–63, 6640 2023. DOI: 10.1126/science.adg6881.

[18] C. U. Hail, M. Foley, R. Sokhoyan, L. Michaeli, and H. A. Atwater, "High quality factor metasurfaces for two-dimensional wavefront manipulation," *Nature Communications*, vol. 14, p. 8476, 1 2023. DOI: 10.1038/s41467-023-44164-4.

[19] C. Guo, H. Wang, and S. Fan, "Squeeze free space with nonlocal flat optics," *Optica*, vol. 7, p. 1133, 9 2020. DOI: 10.1364/OPTICA.392978.

[20] A. C. Overvig, S. A. Mann, and A. Alù, "Thermal metasurfaces: Complete emission control by combining local and nonlocal light-matter interactions," *Physical Review X*, vol. 11, p. 021 050, 2 2021. DOI: 10.1103/PhysRevX.11.021050.

[21] S. Keren-Zur, L. Michaeli, H. Suchowski, and T. Ellenbogen, "Shaping light with nonlinear metasurfaces," *Advances in Optics and Photonics*, vol. 10, p. 309, 1 2018. DOI: 10.1364/AOP.10.000309.

[22] W. T. Chen, A. Y. Zhu, and F. Capasso, "Flat optics with dispersion-engineered metasurfaces," *Nature Reviews Materials*, vol. 5, pp. 604–620, 8 2020. DOI: 10.1038/s41578-020-0203-3.

[23] H. Cai, S. Srinivasan, D. A. Czaplewski, A. B. F. Martinson, D. J. Gosztola, L. Stan, T. Loeffler, S. K. R. S. Sankaranarayanan, and D. López, "Inverse design of metasurfaces with non-local interactions," *npj Computational Materials*, vol. 6, p. 116, 1 2020. DOI: 10.1038/s41524-020-00369-5.

[24] J. Jiang and J. A. Fan, "Global optimization of dielectric metasurfaces using a physics-driven neural network," *Nano Letters*, vol. 19, pp. 5366–5372, 8 2019. DOI: 10.1021/acs.nanolett.9b01857.

[25] O. Y. Long, C. Guo, W. Jin, and S. Fan, "Polarization-independent isotropic nonlocal metasurfaces with wavelength-controlled functionality," *Physical Review Applied*, vol. 17, p. 024 029, 2 2022. DOI: 10.1103/PhysRevApplied.17.024029.

[26] A. Silva, F. Monticone, G. Castaldi, V. Galdi, A. Alù, and N. Engheta, "Performing mathematical operations with metamaterials," *Science*, vol. 343, pp. 160–163, 6167 2014. DOI: 10.1126/science.1242818.

[27] P. Thureja, R. Sokhoyan, C. U. Hail, J. Sisler, M. Foley, M. Y. Grajower, and H. A. Atwater, "Toward a universal metasurface for optical imaging, communication, and computation," *Nanophotonics*, vol. 11, pp. 3745–3768, 17 2022. DOI: 10.1515/nanoph-2022-0155.

[28] E. Arbabi, A. Arbabi, S. M. Kamali, Y. Horie, M. Faraji-Dana, and A. Faraon, "MEMS-tunable dielectric metasurface lens," *Nature Communications*, vol. 9, p. 812, 1 2018. DOI: 10.1038/s41467-018-03155-6.

[29] A. She, S. Zhang, S. Shian, D. R. Clarke, and F. Capasso, "Adaptive metalenses with simultaneous electrical control of focal length, astigmatism, and shift," *Science Advances*, vol. 4, 2 2018. DOI: 10.1126/sciadv.aap9957.

[30] S. Doshi, A. Ji, A. I. Mahdi, S. T. Keene, S. P. Selvin, P. Lalanne, E. A. Appel, N. A. Melosh, and M. L. Brongersma, "Electrochemically mutable soft metasurfaces," *Nature Materials*, vol. 24, pp. 205–211, 2 2025. DOI: 10.1038/s41563-024-02042-4.

[31] R. Sokhoyan, C. U. Hail, M. Foley, M. Y. Grajower, and H. A. Atwater, "All-dielectric high-Q dynamically tunable transmissive metasurfaces," *Laser & Photonics Reviews*, vol. 18, 6 2024. DOI: 10.1002/lpor.202300980.

[32] M. Bosch, M. R. Shcherbakov, Z. Fan, S. Huang, and G. Shvets, "Thermo-optic dielectric metasurfaces for polarization state synthesizers and active lensing," in *Conference on Lasers and Electro-Optics*, Optica Publishing Group, 2020, FTh3Q.8, ISBN: 978-1-943580-76-7. DOI: 10.1364/CLEO_QELS.2020.FTh3Q.8.

[33] P. P. Iyer, R. A. DeCrescent, T. Lewi, N. Antonellis, and J. A. Schuller, "Uniform thermo-optic tunability of dielectric metalenses," *Physical Review Applied*, vol. 10, p. 044 029, 4 2018. DOI: 10.1103/PhysRevApplied.10.044029.

[34] Y. Kim, P. C. Wu, R. Sokhoyan, K. Mauser, R. Glaudell, G. K. Shirmanesh, and H. A. Atwater, "Phase modulation with electrically tunable vanadium dioxide phase-change metasurfaces," *Nano Letters*, vol. 19, pp. 3961–3968, 6 2019. DOI: 10.1021/acs.nanolett.9b01246.

[35] Y. Wang, P. Landreman, D. Schoen, K. Okabe, A. Marshall, U. Celano, H.-S. P. Wong, J. Park, and M. L. Brongersma, "Electrical tuning of phase-change antennas and metasurfaces," *Nature Nanotechnology*, vol. 16, pp. 667–672, 6 2021. DOI: 10.1038/s41565-021-00882-8.

[36] S. Abdollahramezani, O. Hemmatyar, M. Taghinejad, H. Taghinejad, A. Krasnok, A. A. Eftekhar, C. Teichrib, S. Deshmukh, M. A. El-Sayed, E. Pop, M. Wuttig, A. Alù, W. Cai, and A. Adibi, "Electrically driven reprogrammable phase-change metasurface reaching 80% efficiency," *Nature Communications*, vol. 13, p. 1696, 1 2022. DOI: 10.1038/s41467-022-29374-6.

[37] M. Cotrufo, S. B. Sulejman, L. Wesemann, M. A. Rahman, M. Bhaskaran, A. Roberts, and A. Alù, "Reconfigurable image processing metasurfaces with phase-change materials," *Nature Communications*, vol. 15, p. 4483, 1 2024. DOI: 10.1038/s41467-024-48783-3.

[38] A. D. Francescantonio, A. Sabatti, H. Weigand, E. Bailly-Rioufreyt, M. A. Vincenti, L. Carletti, J. Kellner, A. Zilli, M. Finazzi, M. Celebrano, and R. Grange, "Efficient GHz electro-optical modulation with a nonlocal lithium niobate metasurface in the linear and nonlinear regime," *Nature Communications*, vol. 16, p. 7000, 1 2025. DOI: 10.1038/s41467-025-62072-7.

[39] S. Dagli, J. Shim, H. C. Delgado, H. B. Balch, S. Abdollahramezani, C.-Y. Chen, V. Dolia, E. Klopfer, J. Dixon, J. Hu, B. Ogunlade, J.-H. Song, M. L. Brongersma, D. Barton, and J. A. Dionne, "GHz-speed wavefront shaping metasurface modulators enabled by resonant electro-optic nanoantennas," *Advanced Materials*, vol. 37, 40 2025. DOI: 10.1002/adma.202506790.

[40] H. C. Weigand, Ü.-L. Talts, A.-L. Vieli, V. V. Vogler-Neuling, A. Nardi, and R. Grange, "Nanoimprinting solution-derived barium titanate for electro-optic metasurfaces," *Nano Letters*, vol. 24, pp. 5536–5542, 18 2024. DOI: 10.1021/acs.nanolett.4c00711.

[41] D. Chelladurai, M. Kohli, J. Winiger, D. Moor, A. Messner, Y. Fedoryshyn, M. Eleraky, Y. Liu, H. Wang, and J. Leuthold, "Barium titanate and lithium niobate permittivity and pockels coefficients from megahertz to sub-terahertz frequencies," *Nature Materials*, vol. 24, pp. 868–875, 6 2025. DOI: 10.1038/s41563-025-02158-1.

[42] Y.-W. Huang, H. W. H. Lee, R. Sokhoyan, R. A. Pala, K. Thyagarajan, S. Han, D. P. Tsai, and H. A. Atwater, "Gate-tunable conducting oxide metasurfaces," *Nano Letters*, vol. 16, pp. 5319–5325, 9 2016. DOI: 10.1021/acs.nanolett.6b00555.

[43] A. C. Lesina, D. Goodwill, E. Bernier, L. Ramunno, and P. Berini, "Tunable plasmonic metasurfaces for optical phased arrays," *IEEE Journal of Selected Topics in Quantum Electronics*, vol. 27, pp. 1–16, 1 2021. DOI: 10.1109/JSTQE.2020.2991386.

[44] J. Park, B. G. Jeong, S. I. Kim, D. Lee, J. Kim, C. Shin, C. B. Lee, T. Otsuka, J. Kyoung, S. Kim, K.-Y. Yang, Y.-Y. Park, J. Lee, I. Hwang, J. Jang, S. H. Song, M. L. Brongersma, K. Ha, S.-W. Hwang, H. Choo, and B. L. Choi, "All-solid-state spatial light modulator with independent phase and amplitude control for three-dimensional LiDAR applications," *Nature Nanotechnology*, vol. 16, pp. 69–76, 1 2021. DOI: 10.1038/s41565-020-00787-y.

[45] M. Li, C. U. Hail, S. Biswas, and H. A. Atwater, "Excitonic beam steering in an active van der Waals metasurface," *Nano Letters*, vol. 23, pp. 2771–2777, 7 2023. DOI: 10.1021/acs.nanolett.3c00032.

[46] I.-C. Benea-Chelmus, S. Mason, M. L. Meretska, D. L. Elder, D. Kazakov, A. Shams-Ansari, L. R. Dalton, and F. Capasso, "Gigahertz free-space electro-optic modulators based on Mie resonances," *Nature Communications*, vol. 13, p. 3170, 1 2022. DOI: 10.1038/s41467-022-30451-z.

[47] P. Moitra, X. Xu, R. M. Veetil, X. Liang, T. W. W. Mass, A. I. Kuznetsov, and R. Paniagua-Domínguez, "Electrically tunable reflective metasurfaces with continuous and full-phase modulation for high-efficiency wavefront control at visible frequencies," *ACS Nano*, vol. 17, pp. 16 952–16 959, 17 2023. DOI: 10.1021/acsnano.3c04071.

[48] S.-Q. Li, X. Xu, R. M. Veetil, V. Valuckas, R. Paniagua-Domínguez, and A. I. Kuznetsov, "Phase-only transmissive spatial light modulator based on tunable dielectric metasurface," *Science*, vol. 364, pp. 1087–1090, 6445 2019. DOI: 10.1126/science.aaw6747.

[49] Y. V. Izdebskaya, Z. Yang, V. G. Shvedov, D. N. Neshev, and I. V. Shadrivov, "Multifunctional metasurface tuning by liquid crystals in three dimensions," *Nano Letters*, vol. 23, pp. 9825–9831, 21 2023. DOI: 10.1021/acs.nanolett.3c02595.

[50] G. K. Shirmanesh, R. Sokhoyan, P. C. Wu, and H. A. Atwater, "Electro-optically tunable multifunctional metasurfaces," *ACS Nano*, vol. 14, pp. 6912–6920, 6 2020. DOI: 10.1021/acsnano.0c01269.

[51] J. Pribošek, M. Bainschab, and T. Sasaki, "Varifocal MEMS mirrors for high-speed axial focus scanning: A review," *Microsystems & Nanoengineering*, vol. 9, p. 135, 1 2023. DOI: 10.1038/s41378-022-00481-0.

[52] A. Biswas, M. Srinivasan, K. S. Andrews, A. E. Velasco, E. Alerstam, J. P. Allmaras, E. E. Wollman, S. M. Meenehan, M. W. Wright, and R. Rogalin, "Overview of the deep space optical communications (DSOC) technology demonstration," in *Free-Space Laser Communications XXXVII*, H. Hemmati and B. S. Robinson, Eds., SPIE, Mar. 2025, p. 21, ISBN: 9781510684584. DOI: 10.1117/12.3043966.

Chapter 2

INDIUM TIN OXIDE: A COMMON MATERIAL WITH UNCOMMON PROPERTIES

This chapter describes the material, indium tin oxide (ITO), which is a commonly used material in many fields of science and engineering due to its favorable optical and electrical properties, ease of deposition, and wide range of tunability. The following three chapters describe metasurface devices that contain and rely upon the unique properties of ITO. Here, we set the stage by first describing the structure of ITO as well as how it is typically deposited and characterized. Then, we describe the deposition and post-treatment processes that we have developed for ITO as well as details of how it interacts with other materials.

2.1 General properties

Indium tin oxide (ITO) is an n-type degenerately doped semiconductor with a band gap of ~3.5–4.3 eV [1] which is transparent in the visible and near-infrared (near-IR). It is ubiquitous in consumer optoelectronic devices such as photovoltaics [2] and displays [3] in which it is used as a transparent electrical contact. Its band gap is expanded by the Burstein-Moss effect in which the Fermi-level of a highly doped semiconductor is pushed into the conduction band due to the filling of low energy states in the conduction band [1]. It is of a class of materials known as transparent conducting oxides (TCOs) which also includes materials such as Al or Ga doped ZnO, F or B doped SnO_2, and CdO [4]. ITO has been studied extensively due to its interesting combination of high electrical conductivity and low optical absorption. In addition, it exhibits a zero-crossing point in the real part of its permittivity which is referred to as the epsilon-near-zero (ENZ) point [5], [6]. Other interesting properties of ITO include its ultrafast nonlinear optical response [7], [8] and magneto-optic response [9].

ITO is typically deposited as Sn-doped In_2O_3 via many different techniques such as sputtering, evaporation, atomic layer deposition (ALD), and sol-gel processing [10]. Of these deposition methods, radiofrequency (RF) magnetron sputtering is the most common due to a favorable tradeoff between deposition rate, film quality and uniformity, film tunability, capability for large area processing, and low cost. In RF magnetron sputtering of ITO, a sputtering target containing a mix of Sn_2O_3 and

In_2O_3 is often used, and is sputtered in an environment of Ar and O_2 [11]. During deposition, the O_2 flow rate and substrate temperature can be used to control the electronic and optical properties of the film [12]. Post-deposition annealing can provide tunability [13].

The free carriers in ITO are contributed from In donors and oxygen vacancies. While the concentration of In donors is intrinsic to the film, the density of oxygen vacancies can be changed after deposition. In most cases, the carrier concentration of ITO increases as oxygen vacancies increase. Thus, depositions with a low (high) oxygen flow rate tend to result in films with a high (low) oxygen vacancy concentration and, thus, a high (low) carrier concentration. This trend, however, only holds within a certain region of the complex parameter space that is created by all other sputtering conditions such as substrate temperature, pressure, and power. Other factors such as film morphology, grain size, and other possible impurity dopants can affect observed trends of carrier concentration with oxygen flow rate during deposition.

The optical response of ITO in the visible and near-IR can be described by the Drude-Lorentz model [14], [15], [16] given by

$$\varepsilon(\omega) = \varepsilon_\infty - \frac{\omega_p^2}{\omega^2 + i\omega\Gamma} \tag{2.1}$$

where ε is the complex permittivity of ITO, ε_∞ is the high-frequency permittivity, and ω is the angular frequency of incoming light. The plasma frequency, ω_p, and damping coefficient, Γ, are given by

$$\omega_p^2 = \frac{Nq^2}{\varepsilon_0 m_e^*} \tag{2.2}$$

and

$$\Gamma = \frac{q}{m_e^* \mu} \tag{2.3}$$

where N is the bulk carrier concentration, q is the charge of an electron, ε_0 is the permittivity of free space, m_e^* is the effective mass of an electron in ITO, and μ is the electron mobility in ITO. Typical values of the Drude-Lorentz parameters are provided in Table 2.1.

N	μ	ε_∞	m_e^*
$10^{18} - 10^{21}\ cm^{-3}$	$10 - 100\ cm^2/Vs$	3–5	$0.25 - 0.5 m_e$

Table 2.1: Common Drude-Lorentz parameters for ITO films.

2.2 Characterization

The characterization of ITO films has varied significantly across many different studies. Often, some parameters in the Drude-Lorentz model are assumed to be a fixed value, leaving fewer parameters to be fit and simplifying the characterization process. For example, ε_∞ is often assumed to be 3.9 and m_e^* is taken to be some fixed value between 0.25 and 0.35 [15], [16]. While the Drude-Lorentz model can be parameterized in different ways, for this chapter and throughout this thesis, we will use the four parameters presented in Table 2.1 — N, μ, ε_∞, and m_e^* — to describe the Drude-Lorentz model, and thus the permittivity of ITO. Additionally, the film thickness is an important parameter which must be accurately measured. Thus, we have five parameters to fully describe the optical response of an ITO film. It can be very difficult to measure all of these parameters independently, which is why many works assume some of the values to be fixed. Figure 2.1 graphically depicts a series characterization measurements that can provide all five desired parameters. The thickness, t, of the film can be accurately measured using atomic force microscope (AFM) or profilometer, by first patterning a step-edge in the ITO film. Then, the carrier concentration, N, and mobility, μ, can be directly measured using Hall effect measurements and dividing by the measured film thickness. Finally, the high-frequency permittivity, ε_∞, and effective mass, m_e^*, are much more difficult to measure. For example, effective mass can be measured through the measurement of cyclotron frequency, but this is an involved and time-consuming measurement [17]. Thus, these final two parameters can be ellipsometrically fit to a Drude-Lorentz model since t, N, and μ are already known. However, it should be noted that the wavelength range used for fitting ellipsometry data is important for obtaining an accurate result. Ideally, the ENZ wavelength should fall within the measured and fitted bandwidth as this provides a strong resonant feature in Ψ and Δ with which to fit the remaining parameters.

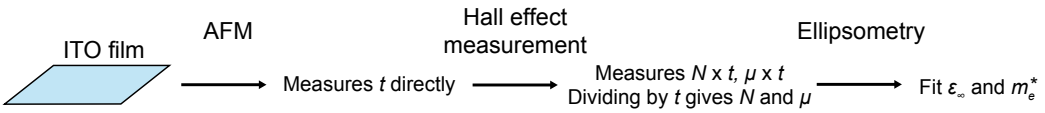

Figure 2.1: Characterization path for obtaining all Drude-Lorentz parameters for a thin film of ITO.

While the in-depth characterization described above can provide an accurate measurement of the permittivity of ITO, it is time consuming and is difficult to use when ITO is sandwiched between other materials, as is often the case in a final active

metasurface device. The final properties of ITO after it has been processed in a full device stack of materials are important and are often vastly different than they were immediately after deposition. For example, it is known that the carrier concentration of ITO increases after ALD Al_2O_3 is grown on top of the ITO [18]. This change in ITO carrier concentration can be very difficult to measure with Hall measurements as the ITO and Al_2O_3 must be patterned in such a way to allow electrical contact to the ITO. Thus, with the need for a fast and reliable method to characterize ITO thin films on various substrates and underneath various other materials, in this thesis, we relied entirely on ellipsometry to characterize our ITO. While this approach does not directly measure each parameter in the Drude-Lorentz model, it can provide an accurate fit as long as the ellipsometric spectrum contains the ENZ resonance. Figure 2.2 demonstrates the importance of using an appropriate wavelength range when collecting ellipsometry data. It shows the data collected from two different

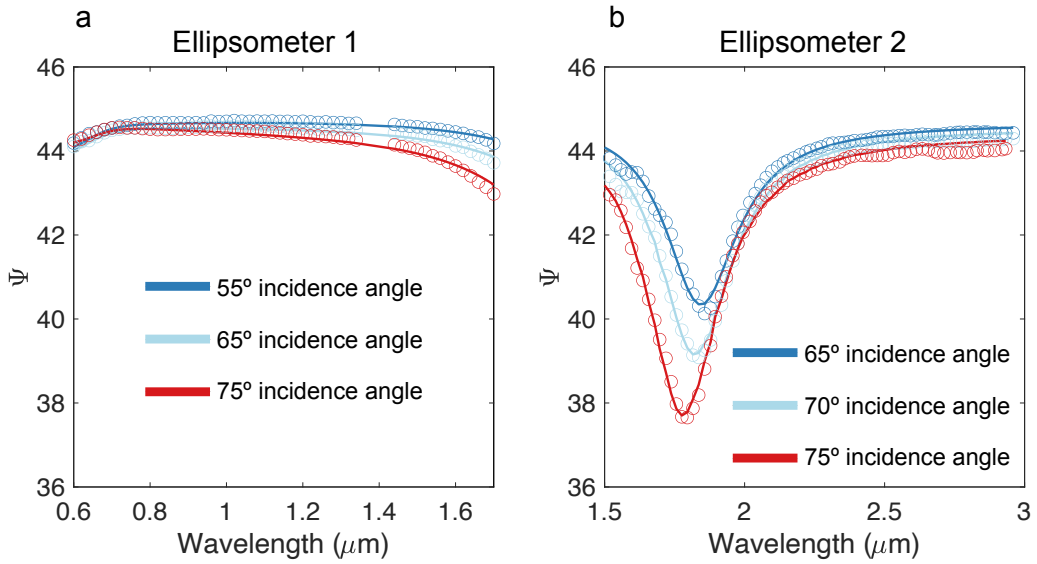

Figure 2.2: Ellipsometric scans of the same ITO film using different bandwidths. (a) Measured (circles) and fitted (dashed lines) raw Ψ for an ITO film using our ellipsometer with a wavlength range from 300 – 1700nm. (b) Measured (circles) and fitted (dashed lines) raw Ψ for the same ITO film in (a) using our ellipsometer with a wavlength range from ~1.5μm – 40μm. We plot a limited wavelength range here to highlight the ENZ resonance of the ITO

ellipsometers available in our lab: One with a wavelength range from 300 – 1700 nm (Fig. 2.2a) and another from ~1.5μm – 40μm (Fig. 2.2b). For the measured ITO film, with a carrier concentration of ~3x10^{20} cm^{-3}, the ENZ wavelength is ~2.3 μm. The ENZ resonance is visible as a strong resonance dip in the raw ellipsometric Ψ data, but the full feature is only visible in the extended wavelength range ellip-

someter. As a result, we can obtain much more accurate Drude-Lorentz model fits using our extended wavelength range ellipsometer as all of the unbiased ITO films of interest in our work have ENZ wavelengths beyond 2 μm. This effect is exaggerated for ITO films with ENZ wavelengths in the midwave and even longwave-IR, which exhibit completely flat features in Ψ and Δ in the wavelength range of our visible ellipsometer. Throughout the remainder of this thesis, we primarily characterize our ITO solely using ellipsometry scans across the near, mid, and longwave-IR.

2.3 Development of a repeatable deposition procedure

As discussed in previous sections, the deposition of ITO through RF magnetron sputtering can allow great tunability of film properties as a function of deposition conditions such as pressure, power, substrate temperature, and oxygen flow rate. This has made sputtering the preferred deposition method for ITO. This tunability, however, also results in an extremely sensitive deposition for which repeatability is difficult to achieve. For the ITO-based active metasurfaces presented later in this thesis, the required properties of ITO (e.g. carrier concentration) must be within ~10% of the designed value. This is an extremely high level of accuracy and precision which is required from such a sensitive sputtering process. This section outlines our final process used to fabricate ITO films with such accuracy and details how we arrived at our final process. It should be noted that there are many possible unknown variables such as chamber contaminants from the deposition of previous materials that may result in the trends and values that we observe from our sputtering system. Thus, the exact conclusions here may not necessarily apply to other sputtering systems.

As a first experiment, we varied the oxygen flow rate during deposition while keeping all other parameters constant. Table 2.2 outlines the deposition conditions used for this initial series of tests. It should be noted that in our sputterer, we have control

Power	Pressure	Substrate Temperature	Ar/O_2 Flow Rate Ratio
100 W	3 mT	Room Temperature	Variable

Table 2.2: ITO sputtering parameters. The substrate temperature was not explicitly set and thus would fluctuate with room temperature

over the flow rate of a "pure" (99.995%) Ar gas and a mixture of Ar/O_2 in a 90/10 weight % mix. For all ITO depositions presented in this thesis, the flow rate of "pure" Ar was kept at 20 sccm while the flow rate of the Ar/O_2 mixture was varied.

All values presented here will be expressed as a ratio of the total flow rate of Ar to O_2. Additionally, we use an ITO target purchased from Kurt J. Lesker which consists of a 90/10 weight % mix of In_2O_3/SnO_2.

Our first experiment consisted of the deposition of two ITO films with fixed Ar/O_2 flow rate ratios each day for three consecutive days. After these three days, each film was measured with ellipsometry. Table 2.3 shows the results of this experiment by only plotting the fitted carrier concentration for simplicity. At first glance, the results may indicate that changing the oxygen flow rate from a ratio of 0.032 to 0.042 results in a large increase in carrier concentration and that this effect was reasonably repeatable across three different days of depositions.

Deposition Day	Ar/O_2 Flow Rate Ratio	Carrier Concentration $[cm^{-3}]$
1	0.032	$0.31x10^{20}$
1	0.042	$2.73x10^{20}$
2	0.032	$1.15x10^{20}$
2	0.042	$2.64x10^{20}$
3	0.032	$0.75x10^{20}$
3	0.042	$2.61x10^{20}$

Table 2.3: ITO deposition repeatability experiment. Two ITO films were grown each day for three consecutive days and the carrier concentration was measured through ellipsometry.

However, to test this hypothesis, we deposited three films on Day 4 with O_2 flow rates of 0.032, 0.042, and 0.032, respectively. Thus, if our initial hypothesis was correct, we would expect the first carrier concentration to be low, the second high, and the third low again. Table 2.4 summarizes the results from the final day of this experiment. We see that, contrary to our hypothesis, the third deposition on Day 4 actually had higher carrier concentration than Deposition 2. Thus, we concluded that the effect of waiting one day had a stronger effect on the carrier concentration than changing the flow rate from an Ar/O_2 ratio of 0.032 to 0.042.

To address the abnormal film properties for the first deposition of each day, we deposited three ITO films in one day with the same Ar/O_2 flow rate ratio. However, before every ITO deposition, we sputtered a pure titanium target in an Ar environment for one hour. Titanium is known to be an effective getter for deposition

Deposition Day	Ar/O_2 Flow Rate Ratio	Carrier Concentration $[cm^{-3}]$
1	0.032	$0.24x10^{20}$
2	0.042	$2.29x10^{20}$
3	0.032	$2.60x10^{20}$

Table 2.4: ITO deposition repeatability experiment – Day 4. Three ITO films were grown on Day 4 and the carrier concentration was measured through ellipsometry.

systems and helped to decrease the chamber base pressure by a factor of ~4. The exact deposition parameters used to sputter Ti are listed in Table 2.5.

Power	Pressure	Substrate Temperature	Ar Flow Rate	Deposition Time
150 W	5 mT	Room Temperature	20 sccm	1 hour

Table 2.5: Ti sputtering parameters. The substrate temperature was not explicitly set and thus would fluctuate with room temperature

The results of including a Ti deposition before each ITO deposition are shown in Table 2.6. These depositions indicate a much better repeatability between each deposited film, and we no longer measure significantly lower carrier concentrations for the first deposition of the day. This result was very useful in our device processing as it allowed us to deposit films at any time of the day and achieve more reliable carrier concentrations of ITO films.

Deposition Day	Ar/O_2 Flow Rate Ratio	Carrier Concentration $[cm^{-3}]$
5	0.1	$2.89x10^{20}$
5	0.1	$3.52x10^{20}$
5	0.1	$3.34x10^{20}$

Table 2.6: ITO deposition repeatability experiment – Ti Gettering. Three ITO films were grown successively on one day and the carrier concentration was measured through ellipsometry.

Although we had improved the repeatability of our ITO deposition process, we still did not have the ~10% precision which was needed for our active metasurfaces. After some experimenting with different possible processes, we determined that this precision was too difficult to achieve directly in our sputtering chamber, given the

parameters that we can control. Thus, we turned to post-deposition annealing to fine-tune the ITO properties after deposited.

2.4 Post-deposition annealing

Post-deposition annealing of ITO is a common technique used by many researchers [14], [19]. This is a useful process as it allows for a wide range of carrier concentrations and can be used to compensate for inherent variability that occurs during deposition. Most previous works anneal ITO at temperatures in the range of ~300 – 500 °C [14], [19]. However, in our work, we use much lower temperature anneals at ~150 °C to achieve greater control and precision over the final carrier concentrations of our ITO films.

As discussed previously, the carrier concentration of ITO is predominantly determined by the concentration of oxygen vacancies. Thus, annealing in an oxygen-rich environment results in a net flow of oxygen into the ITO which will decrease the concentration of oxygen vacancies and decrease the carrier concentration. Consistently, annealing in an oxygen-deficient environment causes oxygen to leave the ITO film, leaving behind more oxygen vacancies, and increasing the carrier concentration. Figure 2.3 shows a cartoon schematic of how oxygen vacancies, and the resulting carrier concentration, are affected when an ITO film is annealed in an air or vacuum environment. We experimentally observed that low temperature

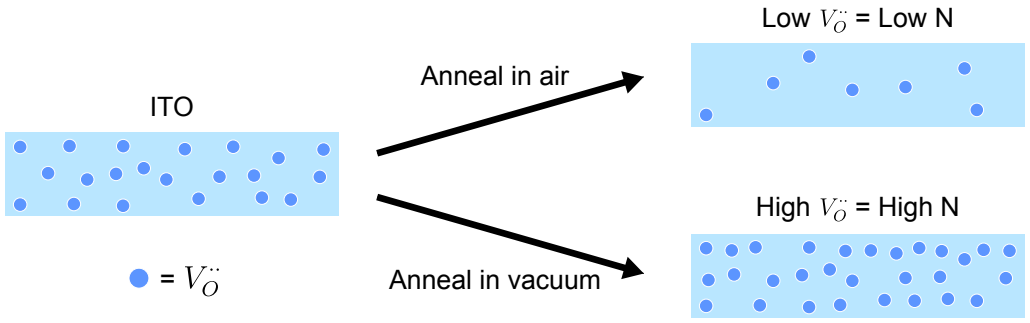

Figure 2.3: Schematic of effect of annealing on ITO carrier concentration. Oxygen vacancies ($V_O^{\cdot\cdot}$), shown as dark blue circles are decreased (increased) when an ITO film is annealed in air (vacuum). This results in a decrease (increase) in N, carrier concentration.

anneals (150 °C) primarily change the carrier concentration of the ITO films without significantly changing other parameters in the Drude-Lorentz model. This is likely a result of the morphology (i.e. film crystallinity, grain size, roughness, density, thickness) remaining constant while the oxygen content varies. It has been previ-

ously reported that ITO films deposited at room temperature via RF sputtering are amorphous and become crystalline once annealed above temperatures of ~300 – 400 °C [20], [21]. Thus, it can be concluded that our 150 °C anneals do not significantly change morphology and predominantly affect the oxygen vacancy concentration of the films.

We first studied the effect of annealing on our ITO films (deposited via RF magnetron sputtering) by consecutively annealing a single ITO film in different oxygen environments (i.e. air and vacuum) and characterizing the change in film properties via infrared ellipsometry as described in Section 2.2. Figure 2.4 shows the real and imaginary parts of the permittivity for a single ITO film directly after deposition (a), after annealing in air (b), and after annealing in vacuum (c). The as-deposited

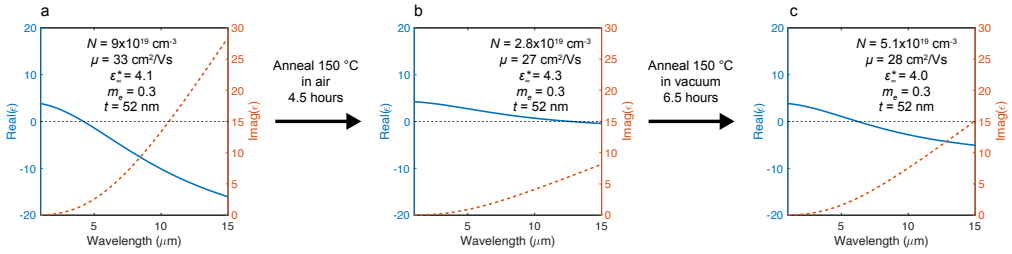

Figure 2.4: ITO permittivity after multiple low-temperature anneals. A single ITO film of thickness ~50 nm was deposited via RF magnetron sputtering. Its permittivity and thickness was characterized via ellipsomtery. Then, the same film was annealed at 150 °C in two different oxygen environments and its permittivity was remeasured after each anneal. (a) The real and imaginary permittivity immediately after deposition. (b) The real and imaginary permittivity immediately after annealing at 150 °C for 4.5 hours in air. (c) The real and imaginary permittivity immediately after annealing at 150 °C for 6.5 hours in vacuum (~1x10^{-5} Torr). For each plot, the extracted Drude-Lorentz parameters from the ellipsometry fit are provided. All parameters were fit except for effective mass, m_e^*, which was fixed at 0.3.

carrier concentration of the ITO film is 9x10^{19} cm^{-3}. After annealing in air (Fig. 2.4b), the carrier concentration significantly decreases to 2.8x10^{19} cm^{-3}. This is consistent with our expectation of anneals in oxygen environments (air) decreasing the oxygen vacancy concentration and overall carrier concentration of the film. Finally, by annealing in vacuum (Fig. 2.4c), the carrier concentration increased to 5.1x10^{19} cm^{-3}. Again, this is consistent with the expectation that annealing ITO in a low-oxygen environment (vacuum) will increase the oxygen vacancies and carrier concentration. Additionally, after each of these anneals, the carrier concentration was the only Drude-Lorentz parameter which was significantly changed, further supporting our claim that such low temperature anneals do not affect morphological

properties of the film. Finally, while we do not show intermediate time data points, by adjusting the time of anneal, the carrier concentration can be precisely tuned between the end values plotted in Fig. 2.4. We believe this is because the time and temperature of our anneals do not allow the films to reach equilibrium. Thus, by changing the time of anneal, we can stop the process before steady-state is reached. This provides us with great tunability in designing passive and active metasurfaces which require precise control over the carrier concentration of ITO films.

2.5 Effect of neighbouring materials on ITO

The previous section described how annealing ITO films in environments of different oxygen content can change how the carrier concentration of the film is affected. Up until now, we have presented this discussion as if a film of ITO is floating in space and is entirely surrounded by air or vacuum. Obviously, this is not the case in real devices. Whenever ITO is deposited on top of a certain substrate or another material is deposited on top of ITO, they will interact with the ITO layer in different ways, especially during the elevated temperatures of anneals. In this section, we will discuss how ITO interacts with surrounding environments other than air and vacuum.

Oxygen-deficient oxides

A common class of materials which are often in contact with ITO in an optoelectronic device is oxides. In the passive and active metasurfaces discussed in this thesis, Al_2O_3 and HfO_2 are the most common as they are used as electrically insulating gate dielectric layers. Depending on the quality of these films, they will either interact strongly or minimally with layers of ITO during deposition and/or during post-deposition anneals. In general, the model which we have used to predict how an oxide film will interact with ITO is visually depicted in Fig. 2.5. We first describe the ITO as a film rich in oxygen vacancy and oxygen interstitial defects. As previously discussed, the oxygen vacancies dictate the carrier concentration of the film. While there can be some material-dependent discrepancies, dielectrics deposited by common microfabrication techniques tend to be oxygen deficient. Thus, we represent the oxide as a film rich in oxygen defects. As discussed in the previous section, when ITO is annealed in an oxygen-deficient environment (e.g. vacuum or oxygen deficient oxide), oxygen diffuses out of the film, leaving behind oxygen vacancies in the ITO, and results in an increase of the carrier concentration.

The model described in Fig. 2.5 is valid for many oxides such as Al_2O_3, HfO_2, TiO_2,

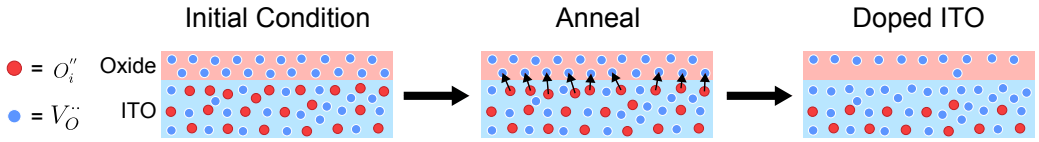

Figure 2.5: Annealing of ITO covered by a low-quality oxide. Oxygen interstitial and oxygen vacancy defects are shown as red and blue circles, respectively. During annealing, oxygen interstitials from the ITO layer diffuse into the oxide to fill available oxygen vacancies and leave behind additional oxygen vacancies in the ITO layer.

and SiO_2 when deposited via physical vapour deposition (PVD) techniques such as electron beam evaporation and sputtering. We have experimentally confirmed that all of these materials, when deposited on ITO via PVD, will result in an increase in carrier concentration of ITO after annealing at 150 °C.

While most oxides tend to be oxygen-deficient, the total concentration of oxygen vacancies can be decreased by either using different deposition techniques such as chemical vapour deposition (CVD), or by first annealing the oxides in air. We explored both of these techniques specifically for Al_2O_3 films. To achieve a higher quality Al_2O_3, we first used thermal atomic layer deposition (ALD) at 150 °C to grow films with a much higher oxygen content. These films were then annealed in air at 200 °C for 24 hours in an attempt to "fill" any oxygen vacancies. We then deposited ITO on top and observed that the properties of the ITO were not significantly impacted by the presence of the Al_2O_3 during anneals. The interaction between these two films is depicted in Fig. 2.6.

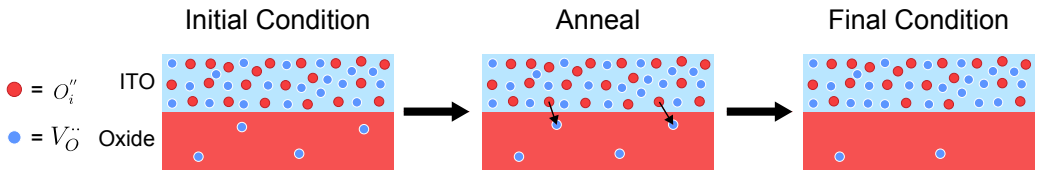

Figure 2.6: Annealing of ITO on top of a high-quality oxide. Oxygen interstitial and oxygen vacancy defects are shown as red and blue circles, respectively. During annealing, some oxygen interstitials from the ITO layer diffuse into the oxide to fill available oxygen vacancies and leave behind oxygen vacancies in the ITO layer. As the high-quality oxide does not have many oxygen vacancies, both films are relatively unchanged by the annealing process.

Although ALD-grown Al_2O_3 will not significantly affect the properties of an adja-

cent ITO film during post-deposition low-temperature anneals, the act of growing the Al_2O_3 on top of a layer of ITO will greatly increase the carrier concentration of the underlying ITO. This effect has been observed in previous works [18], [22] and can be attributed to the first few ALD pulses of Al precursor, trimethylaluminum (TMA), reacting with available oxygen in the ITO film before the second precursor, water, can be reacted with the TMA [18]. When the TMA reacts with the ITO layer, it pulls oxygen out of ITO which creates more oxygen vacancies, thus increasing the carrier concentration. Figure 2.7 plots the ellipsometrically fitted permittivity of an ITO film before (a) and after (b) ALD deposition of Al_2O_3 which increases the carrier concentration by a factor of ~3. It should be noted here that all ALD Al_2O_3 films grown in this thesis used a thermal ALD recipe. Due to the mechanism of the carrier concentration increase, we would expect plasma ALD recipes to affect the ITO films in a similar way.

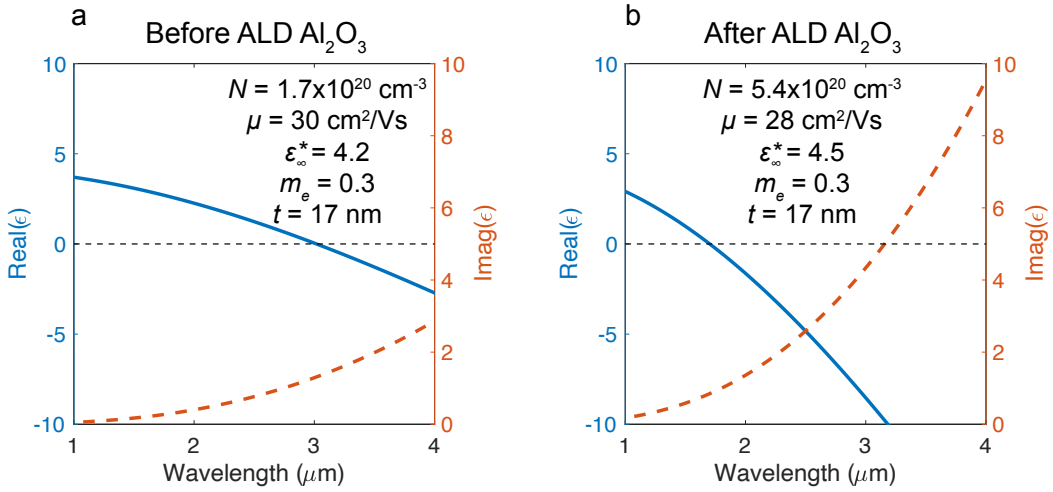

Figure 2.7: Atomic layer deposition of Al_2O_3 on ITO. Ellipsometrically fitted permittivity of an ITO film before (a) and after (b) ALD Al_2O_3 deposition. The full fitted Drude-Lorentz parameters are provided as insets.

Gold

Another common material that can come into contact with ITO-based active metasurfaces is gold, which is often used as an electrical contact, back-reflecting layer, and/or antenna element. These functionalities are often combined due to the favorable properties of gold and plasmonics in the near-IR. However, great care should be taken when gold is in direct contact with an ITO film. We have observed a significant increase in the carrier concentration of an ITO film in contact with gold during anneals at 150 °C. Figure 2.8 shows the measured permittivity for two ITO

films which were deposited in the same deposition on two different substrates: ITO on gold Fig. 2.8a and ITO on ALD grown Al_2O_3 on gold Fig. 2.8b. It was first confirmed (using ellipsometry) that the properties of these ITO films were similar immediately after deposition. Then, both samples were annealed for 3 hours at 150 °C and remeasured. The plotted permittivity in Fig. 2.8 shows the results for each sample after the anneal. The sample which has ITO directly in contact with gold saw a carrier concentration increase of approximately an order of magnitude, while the sample with a layer of ALD-grown Al_2O_3 separating the ITO from the gold had a minimal increase in carrier concentration. We have repeatably observed this phenomenon in all our samples. While the exact mechanism causing this increase in carrier concentration is unknown, we propose that it is caused by the gold forming an interfacial intermetallic compound which pulls more oxygen out of the bulk of the ITO, thus creating more oxygen vacancies and increasing the carrier concentration.

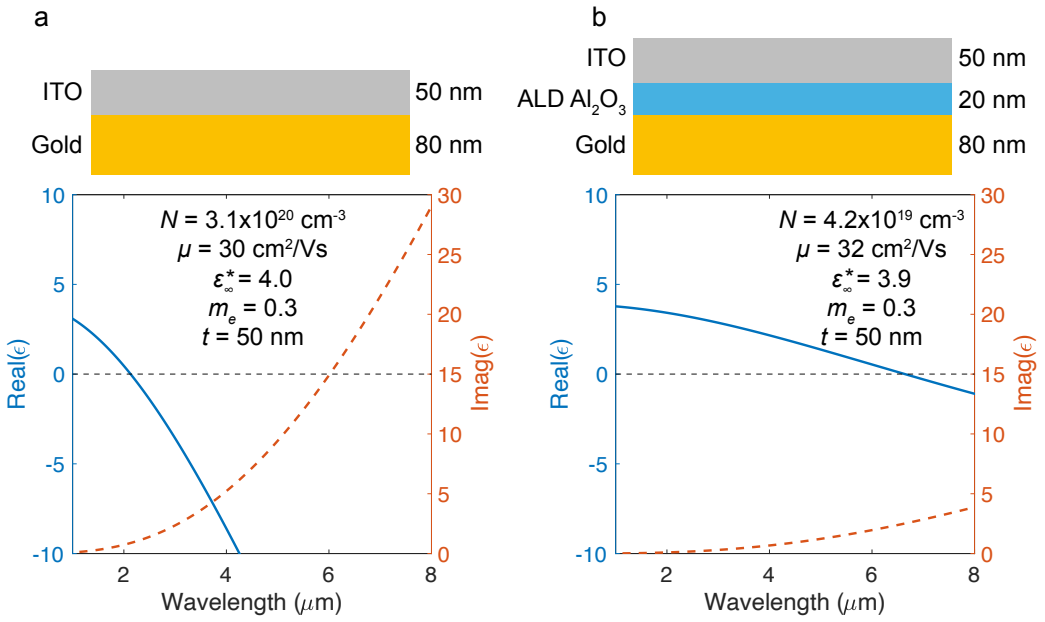

Figure 2.8: Effect of gold on ITO films. Ellipsometrically fitted permittivity of ITO films deposited directly on gold (a) and on an ALD grown layer of Al_2O_3 on gold (b). The ITO on both samples was deposited in the same deposition and the properties of both samples were first confirmed to be similar for the as-deposited films. Then, both samples (a) and (b) were annealed for 3 hours at 150 °C and measured again with ellipsometry. The final permittivity after annealing is plotted here.

Nitrides and oxygen-rich oxides

Thus far, all discussed materials have increased the carrier concentration of ITO, likely by pulling oxygen out of the ITO. A useful alternative to this would be materials that can decrease the carrier concentration of ITO by moving oxygen into the film. Similarly, a material that could be heated to high temperatures while in contact with ITO without changing the carrier concentration of the ITO would be very useful. Possible materials that may allow for this functionality are nitrides and oxygen-rich oxides. While we did not study these materials in great detail, they may be important to creating temperature-stable ITO films in future active metasurfaces, especially when low carrier concentrations are needed. We sputtered AlN and TiN films on top of ITO and studied the change in carrier concentration during annealing. Both films did not cause the carrier concentration to increase as much as previously discussed materials (such as Al_2O_3 and gold), but we still observed a small increase. Additionally, we thermally evaporated MoO_3 (known for being oxygen-rich) on ITO and again measured the change in carrier concentration after annealing. We observed minimal change in carrier concentration after heating. With further process optimization, AlN and MoO_3 may be ideal encapsulant materials for ITO films. In the future, temperature stable active metasurfaces may be enabled by integrating nitrides and/or oxygen-rich oxides.

2.6 A short summary

In summary, this chapter has introduced the material, ITO, by focusing on some of its interesting properties, common characterization techniques, a repeatable deposition procedure, and how ITO can be manipulated by annealing in a wide range of material environments. This provides the necessary background to understand many of the device-level decisions which we made throughout this thesis.

For example, in Section 2.2 we described how we arrived at the decision to only use ellipsometry across a wide wavelength range to characterize our ITO films, but we did not describe exactly how we prepare our samples to make these measurements. For most of our devices, we use Si as a substrate. However, if we simply deposited ITO on top of Si and took an ellipsometry scan from ~1 μm to 20 μm, we would see many resonances associated with the Fabry-Perot cavity created by the Si substrate which is transparent in most of the IR. Additionally, there would likely be some transmitted light which would make the data very difficult to fit. Thus, it would be preferred to have a back-reflecting layer such as gold on top on the Si to make sure that all light is reflected back. However, as discussed in Section 2.5, there could

be strong interactions between the gold and ITO which may change the properties of the ITO, especially during heating. This is not desired if one is studying the effect of annealing ITO in air and vacuum as in both cases the change in the carrier concentration of the ITO will be dominated by the interaction between the ITO and gold. To mitigate this issue, we inserted a film of ALD-grown Al_2O_3 between the ITO and gold which was shown to sufficiently separate the gold and ITO (Fig. 2.8) while not significantly changing the properties of the ITO (Fig. 2.6). This can be further improved by annealing the ALD Al_2O_3 in air at 200 °C for 24 hours to further decrease the concentration of oxygen vacancies before depositing the ITO. Thus, our standard sample preparation, throughout this thesis, for measuring the carrier concentration of an ITO film was: Evaporate 80 nm gold on a Si substrate, deposit ~20 nm Al_2O_3 via ALD, anneal at 200 °C for 24 hours, then deposit ITO. Then, when we wanted to study how other materials such as evaporated Al_2O_3 affected ITO, we would deposited each material on top of this full stack after fully characterizing the initially deposited ITO. This provides further support for our decision to only characterize ITO with ellipsometry because we were able to create complex stacks of materials and precisely measure how each step was affecting the optical properties of ITO. This would be much more complicated with techniques such as Hall effect measurements because complex patterning of materials would be required to ensure that electrical contact is made with the ITO (and only the ITO) as more and more materials are deposited. This process was the standard for observing the trends discussed in this chapter and influenced the final stack of materials used in the devices presented in later chapters.

References

[1] I. Hamberg, C. Granqvist, K.-F. Berggren, B. Sernelius, and L. Engström, "Band-gap widening in heavily Sn-doped In_2O_3," *Physical Review B*, vol. 30, pp. 3240–3249, 6 1984. DOI: 10.1103/PhysRevB.30.3240.

[2] H. Saim and D. Campbell, "Properties of indium-tin-oxide (ITO)/silicon heterojunction solar cells by thick-film techniques," *Solar Energy Materials*, vol. 15, pp. 249–260, 4 1987. DOI: 10.1016/0165-1633(87)90040-2.

[3] A. K. Chaudhari and V. Singh, "A review of fundamental aspects, characterization and applications of electrodeposited nanocrystalline iron group metals, Ni-Fe alloy and oxide ceramics reinforced nanocomposite coatings," *Journal of Alloys and Compounds*, vol. 751, pp. 194–214, 2018. DOI: 10.1016/j.jallcom.2018.04.090.

[4] K. Arya, M. Anjitha, E. Sharika, N. Nair, M. Meenu, P. Sanjeev, V. T. Babu, and S. K. Ram, "Influence of trap densities in ITO thin film on the optical, electrical, and surface plasmon resonance properties," *Journal of Physics: Conference Series*, vol. 2070, p. 012 020, 1 2021. DOI: 10.1088/1742-6596/2070/1/012020.

[5] A. Anopchenko, L. Tao, C. Arndt, and H. W. H. Lee, "Field-effect tunable and broadband epsilon-near-zero perfect absorbers with deep subwavelength thickness," *ACS Photonics*, vol. 5, pp. 2631–2637, 7 2018. DOI: 10.1021/acsphotonics.7b01373.

[6] J. Wu, Z. T. Xie, Y. Sha, H. Y. Fu, and Q. Li, "Epsilon-near-zero photonics: Infinite potentials," *Photonics Research*, vol. 9, p. 1616, 8 2021. DOI: 10.1364/PRJ.427246.

[7] M. Z. Alam, I. D. Leon, and R. W. Boyd, "Large optical nonlinearity of indium tin oxide in its epsilon-near-zero region," *Science*, vol. 352, pp. 795–797, 6287 2016. DOI: 10.1126/science.aae0330.

[8] E. Lustig, O. Segal, S. Saha, E. Bordo, S. N. Chowdhury, Y. Sharabi, A. Fleischer, A. Boltasseva, O. Cohen, V. M. Shalaev, and M. Segev, "Time-refraction optics with single cycle modulation," *Nanophotonics*, vol. 12, pp. 2221–2230, 12 2023. DOI: 10.1515/nanoph-2023-0126.

[9] K. Ikeda, T. Liu, Y. Ota, N. Kobayashi, and S. Iwamoto, "Enhanced magneto-optical effects in epsilon-near-zero indium tin oxide at telecommunication wavelengths," *Advanced Optical Materials*, vol. 12, 2 2024. DOI: 10.1002/adom.202301320.

[10] M. Hossain, A. Salhi, A. Zekri, A. Abutaha, Y. Tong, and S. Mansour, "Studying room temperature RF magnetron-sputtered indium tin oxide (ITO) thin films for large scale applications," *Results in Surfaces and Interfaces*, vol. 18, p. 100 383, 2025. DOI: 10.1016/j.rsurfi.2024.100383.

[11] Z. Yu, I. R. Perera, T. Daeneke, S. Makuta, Y. Tachibana, J. J. Jasieniak, A. Mishra, P. Bäuerle, L. Spiccia, and U. Bach, "Indium tin oxide as a semiconductor material in efficient p-type dye-sensitized solar cells," *NPG Asia Materials*, vol. 8, e305–e305, 9 2016. DOI: 10.1038/am.2016.89.

[12] C.-L. Tien, H.-Y. Lin, C.-K. Chang, and C.-J. Tang, "Effect of oxygen flow rate on the optical, electrical, and mechanical properties of DC sputtering ITO thin films," *Advances in Condensed Matter Physics*, vol. 2018, pp. 1–6, 2018. DOI: 10.1155/2018/2647282.

[13] S. Song, T. Yang, J. Liu, Y. Xin, Y. Li, and S. Han, "Rapid thermal annealing of ITO films," *Applied Surface Science*, vol. 257, pp. 7061–7064, 16 2011. DOI: 10.1016/j.apsusc.2011.03.009.

[14] L. A. M. Astorga, M. Shabaninezhad, H. Northfield, S. Ntais, S. Rashid, E. Lisicka-Skrzek, H. Mehrvar, E. Bernier, D. Goodwill, L. Ramunno, and P. Berini, "Electrically tunable plasmonic metasurface as a matrix of nanoantennas," *Nanophotonics*, vol. 13, pp. 901–913, 6 2024. DOI: 10.1515/nanoph-2023-0796.

[15] Y.-W. Huang, H. W. H. Lee, R. Sokhoyan, R. A. Pala, K. Thyagarajan, S. Han, D. P. Tsai, and H. A. Atwater, "Gate-tunable conducting oxide metasurfaces," *Nano Letters*, vol. 16, pp. 5319–5325, 9 2016. DOI: 10.1021/acs.nanolett.6b00555.

[16] G. K. Shirmanesh, R. Sokhoyan, P. C. Wu, and H. A. Atwater, "Electro-optically tunable multifunctional metasurfaces," *ACS Nano*, vol. 14, pp. 6912–6920, 6 2020. DOI: 10.1021/acsnano.0c01269.

[17] P. Chauhan, C. Thomas, T. Lindemann, G. C. Gardner, J. Gukelberger, M. J. Manfra, and N. P. Armitage, "Measurements of cyclotron resonance of the interfacial states in strong spin–orbit coupled 2D electron gases proximitized with aluminum," *Applied Physics Letters*, vol. 120, 14 2022. DOI: 10.1063/5.0087401.

[18] T. J. Bayer, A. Wachau, A. Fuchs, J. Deuermeier, and A. Klein, "Atomic layer deposition of Al_2O_3 onto Sn-doped In_2O_3: Absence of self-limited adsorption during initial growth by oxygen diffusion from the substrate and band offset modification by Fermi level pinning in Al_2O_3," *Chemistry of Materials*, vol. 24, pp. 4503–4510, 23 2012. DOI: 10.1021/cm301732t.

[19] S. F. J. Blair, J. S. Male, S. A. Cavill, C. P. Reardon, and T. F. Krauss, "Photonic characterisation of indium tin oxide as a function of deposition conditions," *Nanomaterials*, vol. 13, p. 1990, 13 2023. DOI: 10.3390/nano13131990.

[20] N. M. Ahmed, F. A. Sabah, H. Abdulgafour, A. Alsadig, A. Sulieman, and M. Alkhoaryef, "The effect of post annealing temperature on grain size of indium-tin-oxide for optical and electrical properties improvement," *Results in Physics*, vol. 13, p. 102 159, 2019. DOI: 10.1016/j.rinp.2019.102159.

[21] Y. Hu, X. Diao, C. Wang, W. Hao, and T. Wang, "Effects of heat treatment on properties of ITO films prepared by RF magnetron sputtering," *Vacuum*, vol. 75, pp. 183–188, 2 2004. DOI: 10.1016/j.vacuum.2004.01.081.

[22] G. K. Shirmanesh, R. Sokhoyan, R. A. Pala, and H. A. Atwater, "Dual-gated active metasurface at 1550 nm with wide (>300°) phase tunability," *Nano Letters*, vol. 18, pp. 2957–2963, 5 2018. DOI: 10.1021/acs.nanolett.8b00351.

Chapter 3

PLANAR REFLECTIVE GRATINGS ENABLED BY SPATIALLY RESOLVED DOPING OF INDIUM TIN OXIDE THIN FILMS

The material in this chapter was in part presented in

J. Sisler, K. Shayegan, and H. A. Atwater, "Planar gratings enabled by spatially controlled doping of ITO thin films," 2026. In Preparation.

[This chapter is temporarily embargoed.]

Chapter 4

TWO-DIMENSIONAL BEAM-STEERING AND EMISSIVITY MODULATION IN THE MID-INFRARED

The material in this chapter was in part presented in

J. Sisler, P. Pearson, M. Kelzenberg, A. Faraon, and H. A. Atwater, "Electro-optic modulation of coherent and incoherent mid-IR radiation in two-dimensional arrays," 2026. arXiv: 2603.02401 [physics.optics]. [Online].
Available: https://arxiv.org/abs/2603.02401.

[This chapter is temporarily embargoed.]

Chapter 5

ELECTRICALLY TUNABLE SPACE–TIME METASURFACES IN THE NEAR-IR

The material in this chapter was in part presented in [1].

By definition, all active metasurfaces can change their properties in time. However, their response is often slow, limiting operation to the "quasi-static" regime where they switch between different spatial phase gradient configurations but scatter light at the incident wavelength. In this mode, momentum can be imparted to light, enabling shaping of the spatial wavefront, but the optical wavelength cannot be changed. Time-varying media offer an opportunity to overcome this limitation. Rapid modulation of the refractive index of substituent metasurface scatterers creates a temporal interface: an analog to the previously discussed spatial interface. At a temporal interface, the spatial momentum of light is conserved, but the frequency is altered through energy exchange between the incident wave and the time-varying medium [2]. Temporal control of electromagnetic waves has led to the demonstration of exotic optical phenomena such as frequency mixing [3], harmonic beam shaping [4], and breaking of Lorentz reciprocity [5, 6, 7].

Recent experiments demonstrated that combining metasurface spatial and temporal control can offer many unique optical properties [7, 8, 9, 10, 11, 12]. Spatiotemporal modulation of dielectric media interacting with an electromagnetic wave has been studied for decades and has produced nonreciprocal radio frequency (RF) devices capable of functions such as optical isolation [13], pure frequency mixing [14], and amplification of traveling waves [15]. More recently, digital coding architectures, in which biasing of PIN diodes alters the phase response of scattered light, have realized a more general spatiotemporal platform for frequency-multiplexed beam steering and shaping at microwave frequencies [4, 16, 17]. To achieve space-time metasurfaces at optical frequencies, optical pumping of passive phase gradient metasurfaces consisting of nonlinear optical materials has been demonstrated [2, 18, 19]. These systems, however, require the integration of high-power pump pulses, posing challenges for many applications.

In this work, we use electrically tunable metasurfaces operating at 1530 nm and modulated at 1 MHz to demonstrate spatiotemporal control over the scattered light

wavefront and spectrum. We start by collectively driving the metasurface with a time-varying voltage signal to generate frequency sidebands shifted from the incident laser light. Next, we time-delay the applied electrical signal in space to create a frequency-dependent spatial phase profile, enabling diffraction of selected frequencies. Experimentally measured reflectance as a function of frequency and angle confirms that the frequency-shifted light is diffracted while the central frequency signal reflects normally, resulting in excellent beam directivity for frequency-shifted light. We further demonstrate, through the implementation of a real-time experimental optimization, that the frequency spectrum of reflected light can be arbitrarily constructed, and each generated frequency of interest can be independently manipulated in space.

5.1 Realizing spatiotemporal metasurfaces at optical frequencies

Space-time metasurfaces operating at microwave frequencies have been previously demonstrated. While the conceptual framework for space-time modulation is common to both microwave and optical frequency domains, fundamentally different challenges must be overcome to achieve active metasurfaces in the optical domain.

For example, a common method of modulating a single metasurface element in the microwave regime is switching a positive-intrinsic-negative (PIN) diode (~mm-scale) connected to metallic patches between its low resistance "ON" state (forward bias) and high resistance "OFF" state (negative bias) which changes the amplitude and phase of the electromagnetic (EM) field scattered from that element [4, 20]. This technique is very effective at achieving a large modulation at microwave frequencies because the carrier injection is efficient and can be modeled using the Drude model where the change in permittivity will be proportional to $\Delta N/\omega$, where ΔN is the change in carrier concentration and ω is the angular frequency of incident radiation [21]. Thus, at microwave frequencies, a small change in carrier concentration will result in a large change in permittivity, providing significant amplitude and phase modulation.

By contrast, in the optical domain, the higher frequency gives rise to substantially smaller changes in permittivity, so that any material change from carrier accumulation (as in our devices) will result in a very small change in amplitude and phase of scattered light. As a result, active metasurfaces must be coupled to geometric resonances to enhance the light-matter interactions and to obtain significant optical modulation. This is an ongoing challenge in materials selection, device design and

metasurface fabrication. It should also be noted that our approach for electrically tuning phase and amplitude of active optical metasurfaces inherently allows for continuous tunability. By contrast, a single PIN diode can only achieve two different states of phase and amplitude, and multiple diodes must be added to a unit cell to obtain more than two phase or amplitude steps [22]. As a result, our active optical metasurfaces can steer to arbitrary angles with high directivity by exploiting continuous phase tuning without requiring redesign of our subwavelength structures [23].

Another difference is in the nature of electrical interconnects. In the microwave regime, where the wavelength is of order ~10s of mm, individual scatterers can be easily addressed with electrical interconnects that are deeply subwavelength, which does not affect the scattering performance. In the optical domain, the design approach must be fundamentally different because electrical interconnects even with dimensions < 1 μm can significantly affect scattering and wavefront control.

In summary, we note there are distinct challenges in the design and realization of active space-time metasurfaces at optical frequencies as compared to those at microwave frequencies. We address these challenges for electrically modulated space-time metasurfaces at optical frequencies for the first time.

5.2 Design principle

A conceptual illustration of space-time modulation is shown in Fig. 5.1a. The top two plots illustrate how a binary spatial phase profile can create two intensity peaks in the far-field corresponding to the ± 1st diffraction orders (higher orders are cut-off in the plot). Analogously, the middle plots of Fig. 1a show how sinusoidal time-modulation will generate the ± 1st sideband harmonics. By combining these two modulation schemes, a space-time metasurface is realized. The bottom image of Fig. 5.1a shows a schematic of the gate-tunable reflective space-time metasurface used in this demonstration consisting of a one-dimensional (1D) array of nanoantennas, electrically connected with two independent electrodes contacting alternating groups of 12 nanoantennas. The metasurface accepts incoming light at a frequency, ω_{inc}, and all antennas are modulated with an identical waveform at a frequency, ω_{mod}, time-delayed by half a period between the two antenna groups. As a result, reflected light is diffracted and consists of a span of harmonic frequencies given by $\omega_{inc} \pm n\omega_{mod}$, where n is an integer.

To design a spatiotemporal diffraction response, we start by obtaining a relationship

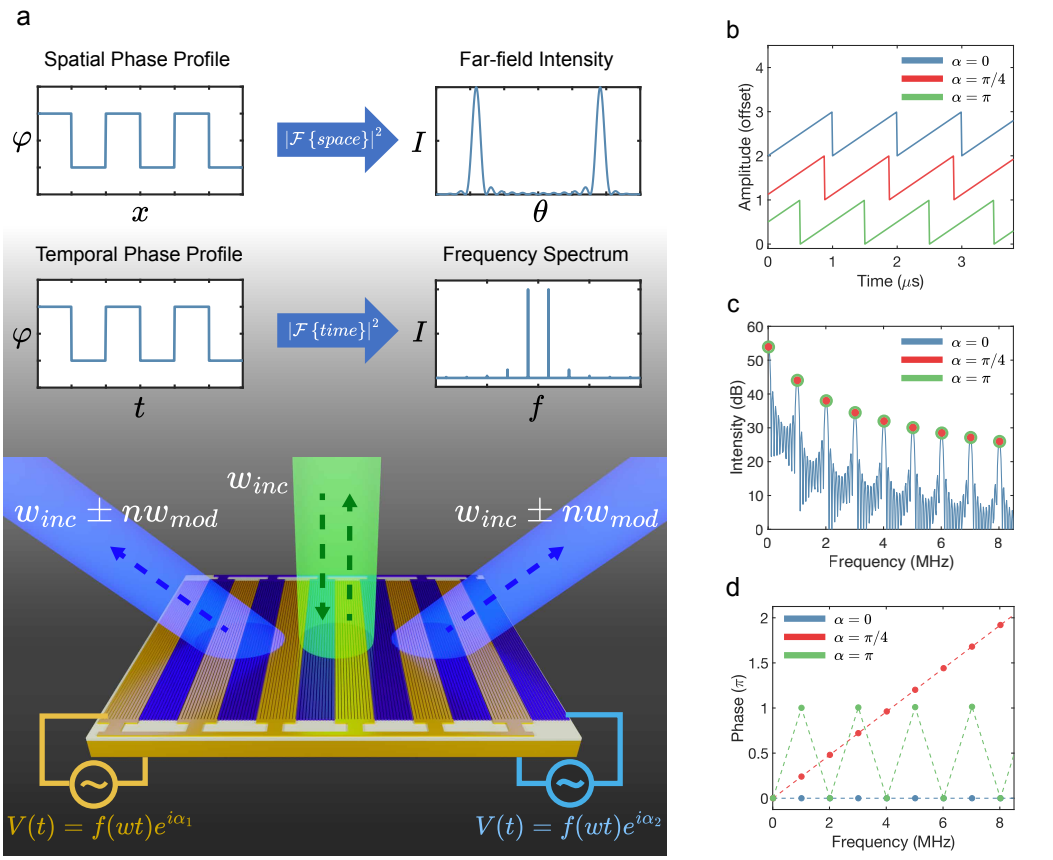

Figure 5.1: Electrically controlled space-time metasurfaces. (a) Upper plots: The magnitude squared of the Fourier transform of a spatial phase gradient (left) provides the far-field intensity profile (right). Middle plots: The magnitude squared of the Fourier transform of a temporal phase gradient (left) provides the frequency spectrum of reflected light (right). Bottom image: 3D visualization of the two-electrode space-time diffracting metasurface. (b) Three example sawtooth waveforms with a frequency of 1 MHz. Each waveform is identical, but has a different initial phase, α. (c) Magnitude squared of the Fourier transform of each waveform in (b). The full spectrum is plotted for $\alpha = 0$, while the intensity at each integer frequency is plotted for $\alpha = \pi/8$ and π for ease of comparison. (d) Phase of the Fourier transform of each waveform in (b) plotted at each harmonic of 1 MHz.

between the reflected amplitude and phase of light at a single wavelength as a function of applied voltage. For quasi-static operation, this relationship would be directly used as a lookup table to determine the required voltage that must be applied across the metasurface. During spatiotemporal modulation, however, multiple frequencies are generated, and the amplitude and phase at each frequency must be considered. This information is obtained by taking the Fourier transform of the time-varying scattered field. Section 5.6 describes this process in more detail.

To illustrate the design principle, Fig. 5.1b shows three time-varying responses of a metasurface exhibiting pure amplitude modulation. Each waveform shape is identical, while the initial phase, α, is varied. Figures 5.1c and 5.1d show the magnitude squared and phase, respectively, of the temporal Fourier transform of each waveform in Fig. 5.1b. As all three signals in Fig. 5.1b have the same shape, the intensity (amplitude squared) spectra are identical. However, the phase spectrum for each waveform is frequency-dependent, given by $\phi(n) = n\alpha$, where n is the harmonic number. If the $\alpha = 0$ and $\alpha = \pi$ waveforms were applied to the two independent electrodes shown in Fig. 5.1a ($\alpha_1 = 0$ and $\alpha_2 = \pi$), there would be a binary $0 - \pi$ phase grating with constant amplitude for odd harmonics, resulting in diffraction of those frequencies. This highlights the unique capability of space-time metasurfaces to decouple phase and amplitude. The shape of the time-varying signal dictates the frequency spectra (i.e., intensity at each frequency) and the time-delay of this signal provides a linear frequency-dependent phase shift. In this example, a metasurface with varying amplitude and constant phase was transformed into a metasurface with constant amplitude and 2π phase coverage at each generated harmonic. It is also important to note that the phase at 0 MHz is identical for all values of α meaning any unmodulated light will not receive a shift in spatial momentum. The ratio of unmodulated to modulated light depends on the accessible phase and amplitude of the metasurface and the selected time-varying signal [11, 12, 24]. Additionally, given the experimental methods used in this work, the unmodulated light is not measured and, thus, is absent from all future plots in this work. Section 5.9 provides detailed calculations of the fraction of unmodulated light in our measurements.

5.3 Device fabrication

Silicon wafers (2 inch diameter) with a 1 μm thermally grown oxide were first cleaned using an RCA 1 and RCA 2 clean. The back gold layer was patterned using photolithography and liftoff in remover PG. The deposition consisted of electron beam (e-beam) evaporation of 5 nm Ti and 80 nm Au electron beam (e-beam) evaporation. Next, the ITO was patterned by photolithography and liftoff in remover PG. The 17 nm ITO deposition used an RF sputterer using a 90/10 wt% In_2O_3/SnO_2 target at 3 mTorr and 100 W while flowing 20 sccm Ar and 4 sccm Ar/O_2 in a 90/10 wt% mix. The HAOL was deposited using a shadow mask via thermal ALD at 150 °C. The deposition consisted of 4 repetitions of 1nm/3nm Al_2O_3/HfO_2 without breaking vacuum to accumulate a total of 16 nm. The nanoantennas were patterned

via e-beam lithography using a bilayer PMMA resist and lifted off in remover PG. The nanoantennas were deposited using the e-beam evaporation of 2 nm Ge and 40 nm Au. Finally, the top contact pads were patterned using photolithography and lifted off in acetone. The contact pads were deposited using e-beam evaporation of 20 nm Ti and 200 nm Au. The final devices were then diced into 1 cm x 1 cm chips and wirebonded to specifically designed PCBs

5.4 Active metasurface characterization

In this work, we use an indium tin oxide (ITO)-based plasmonic metasurface operating in reflection [25, 26, 27, 28]. A camera image of ten devices wire-bonded to a printed circuit board (PCB) is shown in Fig. 5.2a. Figures 5.2b and c show a single metasurface under scanning electron microscope (SEM) and the metasurface cross-section is provided in Fig. 5.2d. ITO, the active material, is modulated in a metal-oxide-semiconductor (MOS) capacitor configuration. Here, ITO acts as a highly doped semiconductor, HAOL — a nanolaminate of alumina (Al_2O_3) and hafnia (HfO_2) [29] — is the gate dielectric, and the gold antennas act as the top metal contact. The bottom gold acts as a backreflecting layer as well as the ITO electrical contact. Under applied voltage, carriers are accumulated in ITO at the ITO-HAOL interface, resulting in modulation of the ITO refractive index. When illuminated with transverse electric (TE) polarized light, a gap plasmon resonance confines light in the ITO and HAOL layers, increasing the optical modulation. Due to the highly confined optical resonance and accumulation of charges, these devices have been shown to demonstrate local behaviour such that their optical response does not depend on the number of unit cells that are electrically addressed [26].

Figure 5.2e shows the measured metasurface reflectance under applied bias. The 1475 nm resonance at –4 V shifts to 1460 nm at 4 V. The operation wavelength throughout this work is 1530 nm, and Fig. 5.2f shows the voltage-dependent reflectance at this wavelength. The phase shift at 1530 nm is negligible and is plotted below. While the relative modulation is larger on resonance, 1530 nm is the shortest wavelength accessible in our experimental setup. It is noteworthy, however, that a device with limited relative reflectance modulation (~8%) and near-zero phase shift, can be used to demonstrate space-time diffraction with excellent directivity, as will be presented in the following sections.

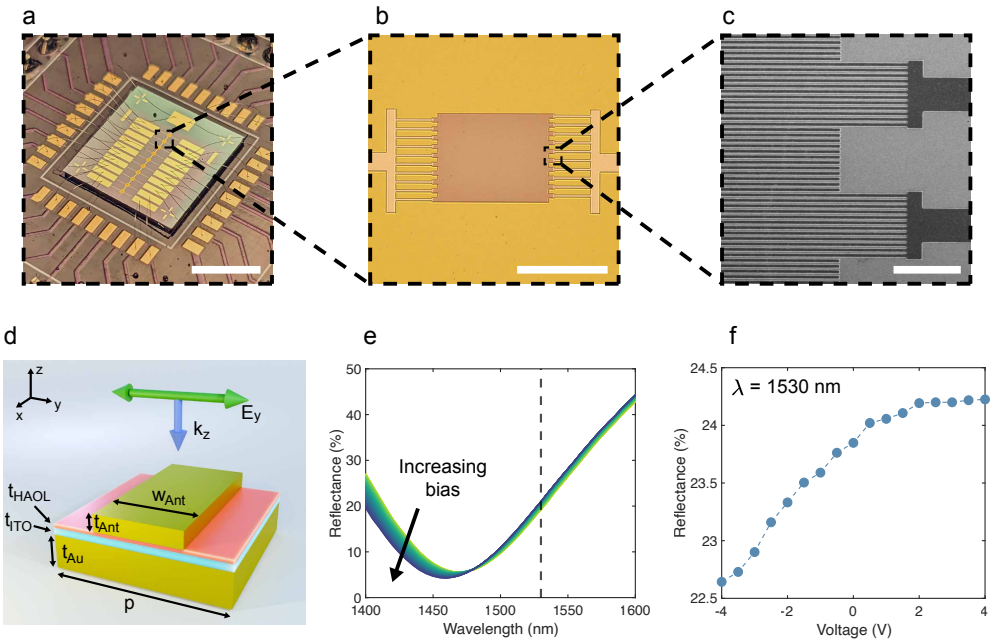

Figure 5.2: ITO-based plasmonic metasurface. (a) Camera image of chip mounted and wire-bonded to a printed circuit board consisting of 10 individual metasurfaces. Scale bar: 5 mm (b) Marked region from (a) showing optical microscope image of a single metasurface. The center region creates a 120 x 120 μm^2 active area of nanoantennas which are contacted by the interconnects on the side of the image. Scale bar: 100 μm. (c) Marked region from (b) showing SEM image of individual nanoantennas. Scale bar: 5 μm. (d) Schematic of metasurface unit cell. The structure is periodic in the y-axis with a period, p, and extends 120 μm in the x-axis. The metasurface is illuminated from the top with a normally incident plane wave polarized in the y-axis. The dimensions labelled are w_{Ant} = 220 nm, t_{Ant} = 40 nm, t_{HAOL} = 16 nm, t_{ITO} = 17 nm, t_{Au} = 80 nm, p = 400 nm. (e) Measured reflectance spectra of metasurface under varying applied bias from –4 to 4 V. The dotted line corresponds to the operation wavelength of 1530 nm used throughout this work. (f) Measured reflectance modulation of the metasurface as a function of applied bias at an operation wavelength of 1530 nm.

Quasi-static phase modulation

Figure 5.3 plots the maximum phase shift achieved by our active metasurface as a function of wavelength. The largest phase shift occurs between λ = 1465 nm and 1470 nm, corresponding to the minimum reflectance measured in Fig. 5.2e. The phase shift of this device at the design wavelength for this work (1530 nm) is near-zero (< 20°). While there is larger amplitude and phase modulation at shorter wavelengths (λ ~1470 nm), we chose to work at λ = 1530 nm because it is the shortest wavelength we could access with sufficient power in our experimental setup. This work could be repeated closer to resonance using the same principles discussed

here and the final results would be identical, but the overall efficiency of the device would be higher. Specifically, there would be a higher ratio of total modulated light to unmodulated light. However, since our measurement technique already filters out unmodulated light, in this work we are still able to show the same principles of space-time modulation and engineer the power sent to each modulated frequency with good signal-to-noise ratio (SNR).

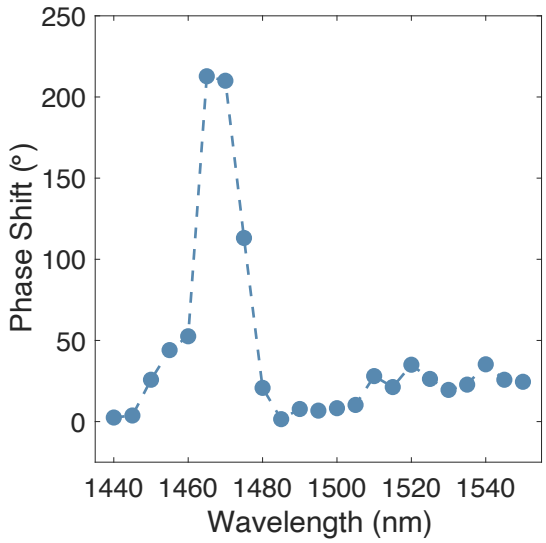

Figure 5.3: Quasi-static phase shift of the active metasurface used in this work. The plotted phase shift is the absolute value of the change in phase between an applied bias of –6 V and 6 V.

It is noteworthy that this work demonstrates space-time diffraction with excellent directivity at each modulated frequency using a device with such limited reflectance and phase modulation. If this device was modulated in the quasi-static regime, it would exhibit very low diffraction efficiency (see Section 5.9). By using space-time modulation, roughly the same total amount of light is diffracted as in the quasi-static case, but the light sent to the $\pm$ 1st orders are separated in frequency from the 0th order (normally reflected light) which allows for easier detection with high SNR. This is a major benefit of space-time metasurfaces.

Frequency-response of ITO-based metasurfaces

Before beginning temporal modulation, it is useful to predict the cutoff frequency of our device. By doing this, we were able to conclude that, in this work, the frequency of modulation is limited by the detection scheme, not the metasurface device. The 3 dB cutoff of the photodiode used is 10 MHz (ThorLabs APD410C) and we chose to

modulate at 1 MHz to ensure that we can sufficiently resolve higher order harmonics without losing collected signal. Since the carrier modulation in ITO occurs in a small layer (< 17 nm) the carrier accumulation occurs very quickly. Previous demonstrations have experimentally demonstrated ITO modulators reaching GHz speeds [30, 31]. Because of this, we do not expect the ITO response time to be a limiting factor at MHz frequencies. A more probable limitation could come from the RC time constant of our driving circuits.

To estimate the frequency response of the interconnects and antennas driving our metasurface, we used a simple RC time-constant estimate based on the geometry of our device. By doing this, we calculate, for one metasurface antenna group (consisting of 156 individual nanoantennas), a resistance of ~2 Ω and a capacitance of ~50 pF resulting in a RC-limited frequency of ~1.6 GHz. A plot of the characteristic frequency of the antenna groups as a function of antenna length is plotted in Fig. 5.4a. The antennas for the metasurfaces in this work are 120 μm long. Next, we examined the frequency response of the fabricated interconnects that electrically address each antenna group. These interconnects are of varying length (~50 μm to 1 mm) and width (~2.5 μm to 20 μm). Figure 5.4b plots the characteristic frequency for these interconnects of varying length and width, by calculating the resistance and self-inductance of the lines. Using these estimates, Fig. 5.4 shows that for all considered dimensions of nanoantennas and interconnects, the characteristic frequency remains above 100 MHz. Therefore, the electrical connections in our device will not limit modulation at 1 MHz.

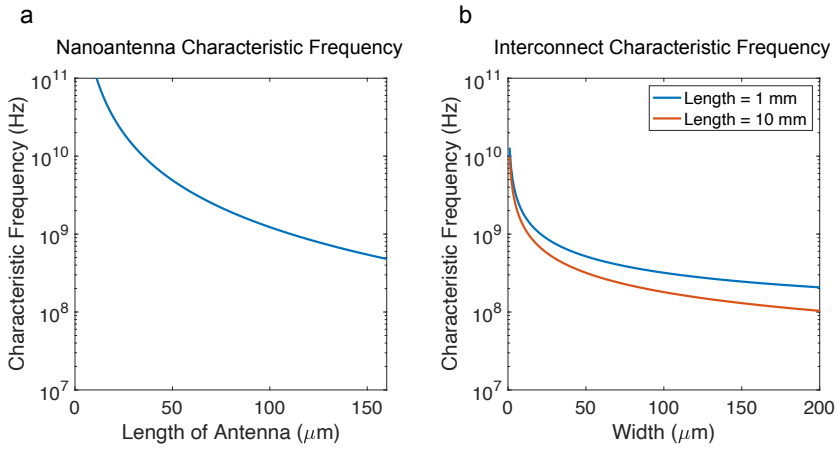

Figure 5.4: Simulated frequency response of metasurface. (a) Characteristic frequency of metasurface nanoantennas as a function of antenna length. (b) Characteristic frequency of interconnects of varying length as a function of interconnect width.

5.5 Temporal waveform optimization

To study the temporal response of the metasurface, we first modulate all antennas in-phase and measured the reflected frequency spectrum using the experimental setup in Fig. 5.5a. The metasurface is illuminated with 1530 nm light and modulated at MHz frequencies with an arbitrary waveform generator (AWG). A fast photodiode connected to a spectrum analyzer captures reflected light. Because the time-responses of the photodiode (~10 MHz) and spectrum analyzer (~1 GHz) are many orders of magnitude slower than the oscillation of the incident laser light (~200 THz), only the MHz frequency sidebands imparted on the 1530 nm light are measured. Therefore, the 1530 nm laser light acts as a carrier wave to study the modulation dynamics of the metasurface, and the intensity of any unmodulated reflected 1530 nm light is not detected. Because the device used in this work operates using amplitude modulation and modest phase modulation, there is significantly more unmodulated light than frequency converted light which limits our total diffraction efficiency to ~0.0036%. This low efficiency is a result of the device used and is not a fundamental limitation of the method presented in this work. Section 5.9 presents an analysis of the total unmodulated light from our metasurface and provides insights into how the total efficiency can be increased. It should be noted that ITO-based modulators have demonstrated modulation speeds up to GHz [30, 31] and, thus, it is the photodiode, not our metasurface, that limits this work to operation at MHz frequencies.

The reflected frequency spectrum can be manipulated by applying standard time-varying waveforms to the metasurface (e.g., sine, square, sawtooth). However, our metasurface exhibits a non-linear reflectance-voltage relationship (Fig. 5.2f), so the reflected frequency spectrum will not match the spectrum of the driving electrical signal. To address this, we incorporate an experimental feedback loop to continuously update the driving waveform until a desired frequency spectrum is measured (Fig. 5.5a). This technique is particularly useful as it compensates for the non-linearities of the metasurface as well as other elements such as the metasurface interconnects, PCB, waveform generator, photodiode, etc. A genetic algorithm optimization was used to fit the amplitude and phase of the first 20 terms in a Fourier series to generate the final driving voltage waveform, using 1 MHz as the fundamental harmonic. As a first demonstration, the applied waveform is optimized to generate only the 1 MHz signal. The top blue curve in Fig. 5.5b shows the measured frequency spectrum when the metasurface is driven with a 1 MHz sine wave. As desired, there is a strong signal at 1 MHz but there is unwanted

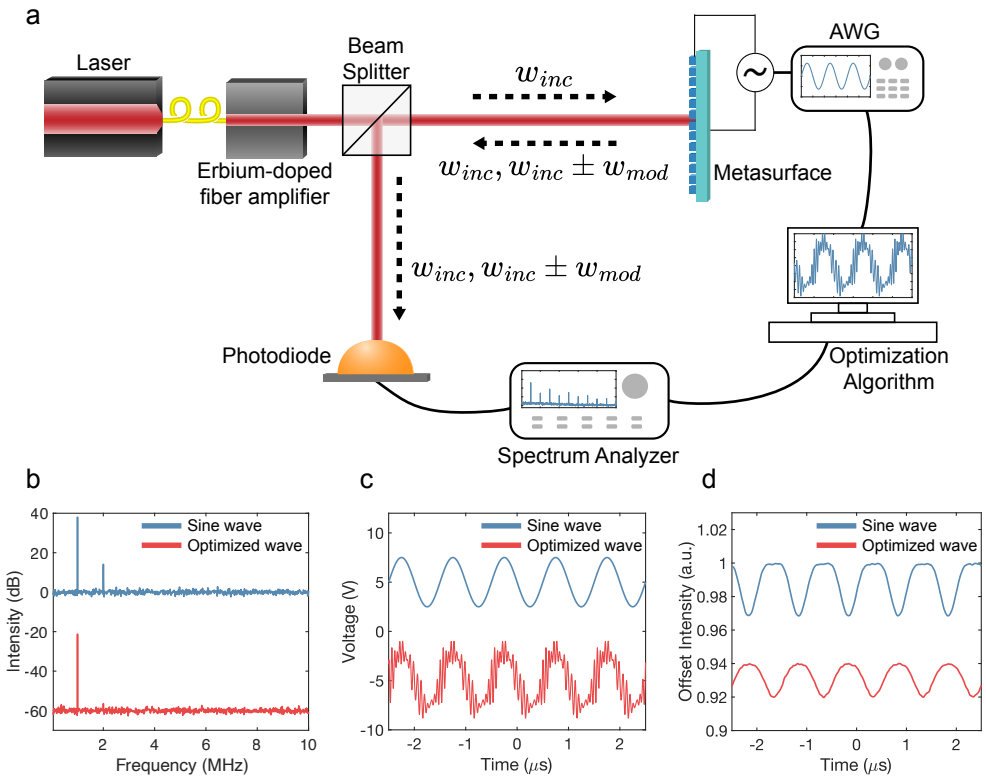

Figure 5.5: Time-modulation and waveform optimization. (a) Schematic of experimental setup. (b) Reflected frequency spectra when metasurface is driven with a 5 V_{p-p} sine wave (blue) and the final optimized waveform (red). (c) Sine (blue) and optimized (red) driving voltage waveforms that were applied to the metasurface to produce the frequency spectra in (b). (d) Measured time-response of the reflectance from the metasurface when driving with the sine (blue) and optimized (red) waveforms from (c).

power at 2 MHz. To suppress this harmonic, the optimization is run with a figure of merit (FOM) defined to maximize the power at 1 MHz while suppressing all other frequencies. Section 5.10 discusses details of the optimization algorithm and FOM selection. The optimization produces a new spectrum (red curve in Fig. 5.5b) that maintains power in the 1st harmonic while greatly reducing the 2nd harmonic. Figure 5.5c shows the corresponding voltage waveforms sent to the AWG for the frequency spectra in Fig. 5.5b. The optimized waveform consists of a maximum frequency component of 20 MHz which is greater than the 3 dB cutoff of the photodiode (10 MHz) and, thus, is partially filtered out in experiment. However, it was found that including these higher frequency components resulted in improved higher-order harmonic suppression. Figure 5.5d plots the measured time-domain reflectance while modulating with a single-frequency sine wave and then optimized wave from

Fig. 5.5c. As expected, the reflectance when driving with a sine wave is significantly distorted. The optimized wave is much closer to a sine wave but is still not perfect because the optimization algorithm can only suppress higher order harmonics into the noise floor of the frequency measurements. To approach a perfect sinusoidal reflectance response, one could integrate the frequency measurements for a longer time, providing better signal-to-noise ratio (SNR) of each higher order harmonic.

5.6 Frequency domain/far-field calculations

To calculate and predict the spatiotemporal response of our metasurface, we make use of a two-dimensional (2D) Fourier transform of the electric field scattered from our metasurface in space and time. As illustrated in Fig. 5.1a, a spatial Fourier transform of the field across our metasurface provides the far-field intensity in space (top plots) and a temporal Fourier transform provides the reflected frequency spectrum (middle plots). By combining these two transforms, we can predict the expected intensity reflected from our metasurface as a function of frequency and angle.

For all calculated intensity plots as a function of frequency and angle, we first start by discretizing the selected driving voltage signal. Figure 5.6a shows an example driving waveform which was used to generate the single 1 MHz signal in Fig. 5.8. Next, using Fig. 5.2f, we calculate the expected reflectance/amplitude from the metasurface as a function of time (Fig. 5.6b). Note: throughout this work, we define reflectance as the magnitude squared of amplitude. At this point, the magnitude squared of the Fourier transform of the time-varying amplitude in Fig. 5.6b would provide the expected frequency-dependent intensity of reflected light. This frequency spectrum is plotted in Fig. 5.6c. Note that this spectrum includes negative frequencies as well as the 0^{th} harmonic. As expected, the signal in the 1^{st} harmonic is multiple orders of magnitude than the higher harmonics (consistent with our measurements) but it is many orders of magnitude smaller than the unmodulated 0^{th} harmonic which is not directly measured in our experiments.

To calculate the full space-time response of our metasurface, we first find the time-varying amplitude for the second antenna group by again using the reflectance/voltage relationship in Fig. 5.2f and the time-varying voltage signal sent to these antennas. Figure 5.6d plots the scattered amplitude of the time-varying field for both antenna groups when modulating in the out-of-phase condition shown in Fig. 5.8b. We can use the two time-varying field profiles from Fig. 5.6d to create a matrix of the

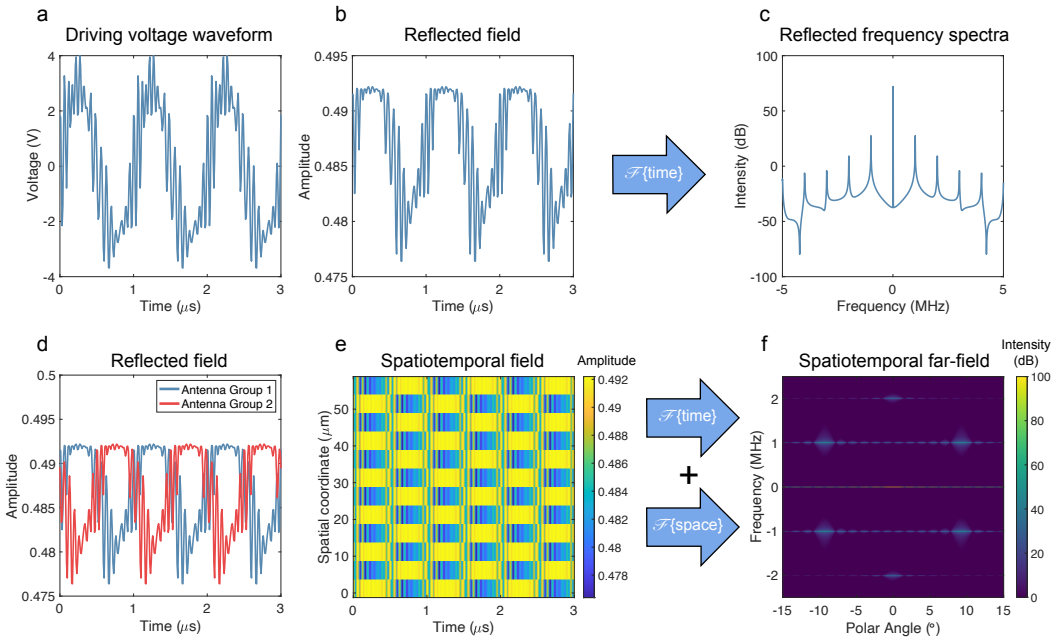

Figure 5.6: Calculation of far-field intensity. (a) Optimized time-varying voltage signal. (b) Amplitude of field reflected from metasurface when all antennas are driven with voltage signal in (a). (c) Magnitude squared of Fourier transform of signal shown in (b) providing reflected frequency spectrum. (d) Amplitude of field reflected from each metasurface antenna group when driving metasurface in out-of-phase condition from Fig. 5.8b. (e) Spatiotemporal scattered field across 6 metasurface periods in space and 3 periods in time for out-of-phase condition in Fig. 5.8b. (f) Magnitude squared of 2D Fourier transform of (e) providing far-field reflected intensity from metasurface as a function of frequency and angle.

scattered field in space and time (Fig. 5.6e). Finally, we take a 2D Fourier transform of this matrix and plot the magnitude squared of the output field in Fig. 5.6f to obtain the expected intensity as a function of frequency and angle. Again, as expected, we see diffraction at the $\pm$ 1$^{\text{st}}$ harmonics while the strongest signal appears at the 0$^{\text{th}}$ harmonic. Since we do not detect the unmodulated signal in experiment, all plots in this chapter are cut off shortly above 0 MHz. Additionally, it should be noted that the Fourier transforms used to compare to measurement in this work include many more temporal periods than are shown here and use padded zeros to improve resolution.

5.7 Diffraction of a single harmonic

As a first step, we demonstrate the spatiotemporal diffraction of a single harmonic.

Experimental setup for space-time measurements

Before we present our space-time measurements, we introduce the experimental setup used to collect the reflectance in space and time. Figure 5.7 shows a schematic of the experimental setup used to obtain the measurements of reflected intensity as a function of frequency and angle presented in Figs. 5.8 and 5.9. Laser light

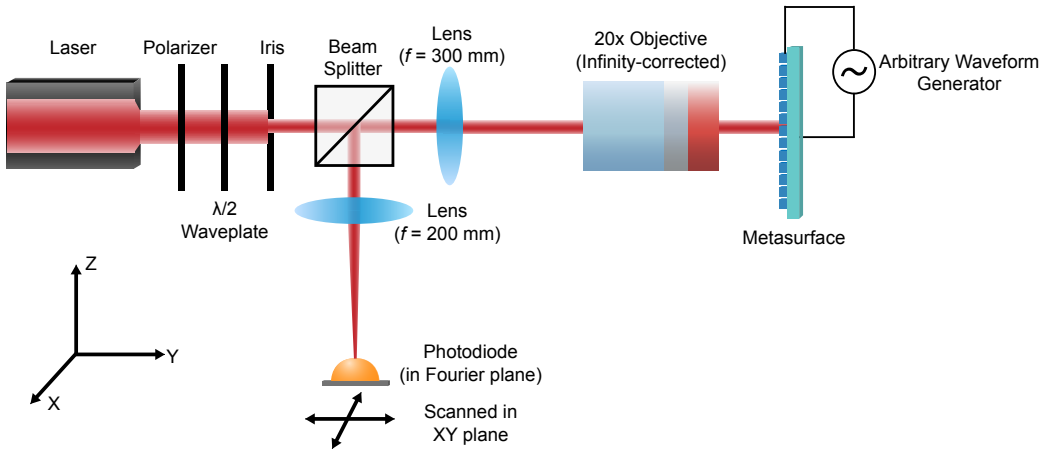

Figure 5.7: Optical setup used for space-time measurements. The metasurface is illuminated with linearly polarized laser light, modulated with an arbitrary waveform at 1 MHz, and the reflected light from the metasurface is measured by a photodiode placed in the Fourier plane, connected to a spectrum analyzer.

with a wavelength of $\lambda = 1530$ nm is emitted from a continuous-wave laser and sent through a polarizer and half-waveplate to control the polarization to be orthogonal to the antennas on the metasurface. Next, an iris decreases the beam size of the laser and it is focused by a 300 mm lens to the back focal plane of a 20x infinity-corrected near-infrared (IR) objective which roughly collimates the laser light on the metasurface. The metasurface is modulated at 1 MHz with an arbitrary wave and the reflected light from the metasurface is collected again by the near-IR objective and 300 mm lens before the light is reflected away from the laser using a beam splitter. Finally, a 200 mm lens is used to focus the light, and a photodiode (connected to a spectrum analyzer) is placed in the Fourier plane after this lens. The photodiode is mounted on a two-axis motorized stage and is scanned in the xy plane (each point corresponds to a different angle of light reflected from the metasurface). At each point in the XY plane, three frequency spectra are collected and averaged. Since the metasurface only diffracts light in one dimension, we would ideally only need to scan the photodiode in one axis, assuming everything is perfectly aligned. However, there is inevitably some misalignment between the direction of diffraction from our

metasurface and the scan direction of our photodiode. Thus, we scan the photodiode in 2D space in the Fourier plane and then extract a line cut that connects the maxima of the two diffracted orders and the 0^{th} order. Using this experimental setup, we collect intensity as a function of frequency and position in the Fourier plane which allows us to generate the intensity versus frequency and angle plots presented in Figs. 5.8 and 5.9.

It should be noted that since the active area of our metasurfaces is ~120x120 μm^2, the 20x objective is needed to first image the metasurface and ensure it is being fully illuminated by the laser. In practice, the optical setup in Fig. 5.7 is first used by removing the 200 mm lens and replacing the photodiode with an IR camera. By doing this, we are able to image the metasurface area with enough magnification to align the beam properly and close the iris to ensure that only the active area of the metasurface is illuminated. Once everything is set up properly, we insert the 200 mm lens to image the Fourier plane and replace the camera with the photodiode. By keeping the 200 mm lens after the beam splitter, we ensure that the metasurface illumination remains the same. Multiple XY scans of the photodiode are also performed at various z-axis positions before a final scan is performed to ensure that the photodiode is placed perfectly in the Fourier plane.

Single-frequency space-time measurements

Space-time metasurfaces can spatially manipulate the wavefront for the generated frequency spectrum. Figures 5.8a and b illustrate two driving schemes under study. In both cases, the metasurface is driven with the optimized waveform from Fig. 5.5 with each antenna group in-phase (Fig. 4a) and half a waveform period (π) out-of-phase (Fig. 4b). The resultant measured frequency spectra at the 0^{th} and $+1^{st}$ diffraction orders are shown for each situation. For the in-phase case, there is no spatial phase profile, and nearly all the reflected 1 MHz signal is in the 0^{th} order. There is a small 1 MHz signal in the $+1^{st}$ diffraction order which is likely caused by the two independent antenna groups having a slightly different amplitude/voltage response. See Section 5.8 for an in-depth discussion on this point. In the out-of-phase case, the 1 MHz signal at the $+1^{st}$ diffraction order is ~12 times greater than the 0^{th} order. The small unwanted signal at the 0^{th} order can be attributed to a change in the average reflectance of the entire metasurface in time. Section 5.8 also addresses this effect.

To further investigate the space-time performance of our metasurface, we employ

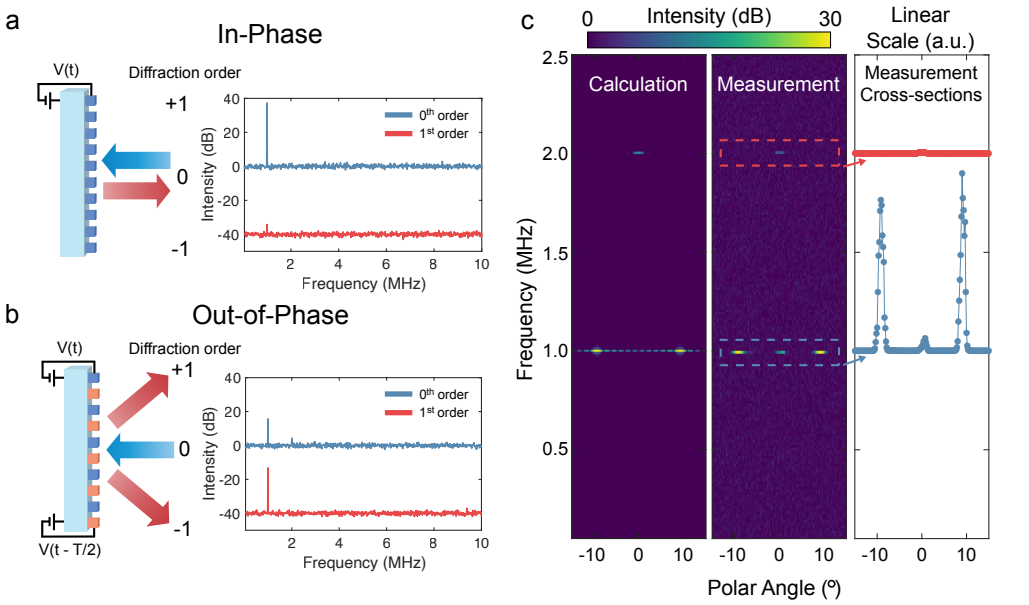

Figure 5.8: Diffraction of a single harmonic. Throughout this figure, the metasurface is modulated with the red optimized voltage waveform from Fig. 5.5(c). (a) All metasurface antennas are modulated in-phase. Left: Schematic of metasurface response. Right: Measured frequency spectra when photodiode is placed at the 0^{th} (blue) and $+1^{st}$ (red) spatial orders. (b) Driving waveform is applied to all metasurface nanoantennas, time delayed by half a period between adjacent nanoantenna groups. Left: Schematic of metasurface response. Right: Measured frequency spectra when photodiode is placed at the 0^{th} (blue) and $+1^{st}$ (red) spatial orders. (c) Metasurface is modulated in the 'Out-of-Phase' condition from (b). Calculated (left) and measured (center) intensity of reflected light as a function of frequency and angle, plotted in log scale. (Right) Spatial intensity cross-sections from center figure, plotted in linear scale at 1 MHz (blue) and 2 MHz (red).

the driving scheme shown in Fig. 5.8b while scanning the photodiode through space, measuring the frequency spectrum at each point, to generate an intensity map of reflected light as a function frequency and angle (Fig. 5.8c). The left panel of Fig. 5.8c shows the predicted response obtained by taking the 2D Fourier transform of the electric field across the metasurface in space and time. The middle panel shows the measured data, and the right panel shows a spatial cross-section of the measured intensity at each integer harmonic of the modulation frequency. While the total amount of diffracted light is limited, 94% of the power is in the $\pm$ 1^{st} diffraction orders at the frequency of interest (1 MHz). This is a significant increase in performance compared to the achievable quasi-static diffraction for this metasurface. Further discussion comparing quasi-static and space-time diffraction is presented in Section 5.9.

5.8 Arbitrary frequency generation and diffractive switching

Now we generalize our method to demonstrate the spatiotemporal diffraction of multiple, arbitrarily selected frequencies.

Multi-frequency space-time measurements

We also demonstrate waveform design to generate arbitrary frequency spectra with individual spatial control over each frequency of interest. First, we target the simultaneous generation of the 3rd and 5th harmonics at equal intensity while suppressing all others. Figure 5.9a plots the measured frequency spectrum for this case, generated using the top blue driving voltage signal in Fig. 5.9b. In the waveform optimization, the fundamental frequency remains at 1 MHz (i.e., the time-domain signal has a period of 1 μs) and the algorithm is left to find a suitable solution (see Section 5.10 for details). Next, the waveform applied to one antenna group is offset by half a period (bottom red line in Fig. 5.9a). By doing this, the phase accumulated at the nth harmonic is equal to $\phi(n) = n\pi$ (Fig. 5.1d). Since both excited harmonics are odd, the phase profile at 3 and 5 MHz obtains the desired binary phase grating for symmetric diffraction. Figure 5.9c shows the calculated (left) and measured (center) response of the metasurface using the two driving waveforms in Fig. 5.9b. The right plot in Fig. 5.9c shows the measured cross-sections at each harmonic.

Next, we generate the first five harmonics with equal power while suppressing all others. Figure 5.9d shows the measured frequency spectrum when the metasurface is driven with the top blue waveform in Fig. 5.9e. In this case, to simultaneously diffract all generated frequency harmonics, one cannot time-delay the driving waveform of one antenna group by half a period because the even harmonics will accumulate a phase shift equal to a multiple of 2π, resulting in a constant spatial phase profile. However, since the optimized driving waveform is constructed from a Fourier series, the phase of each harmonic term can be easily controlled. A new waveform is created for the second group of antennas by offsetting the phase of the first five terms in the driving waveform Fourier series by π. This new waveform is plotted in the lower red curve in Fig. 5.9e. Using the two waveforms in Fig. 5.9e, Fig. 5.9f compares the calculated and measured data. As desired, all five generated harmonics are symmetrically diffracted. Finally, we reuse the optimized waveform for the first five harmonics and arbitrarily decide to diffract only the 2nd and 3rd harmonics. The frequency spectrum and driving waveform are repeated in Figs. 5.9g and 5.9h, respectively. To generate the waveform for the second electrode, we offset the phase of the 2nd and 3rd harmonics by π, providing the bottom red waveform

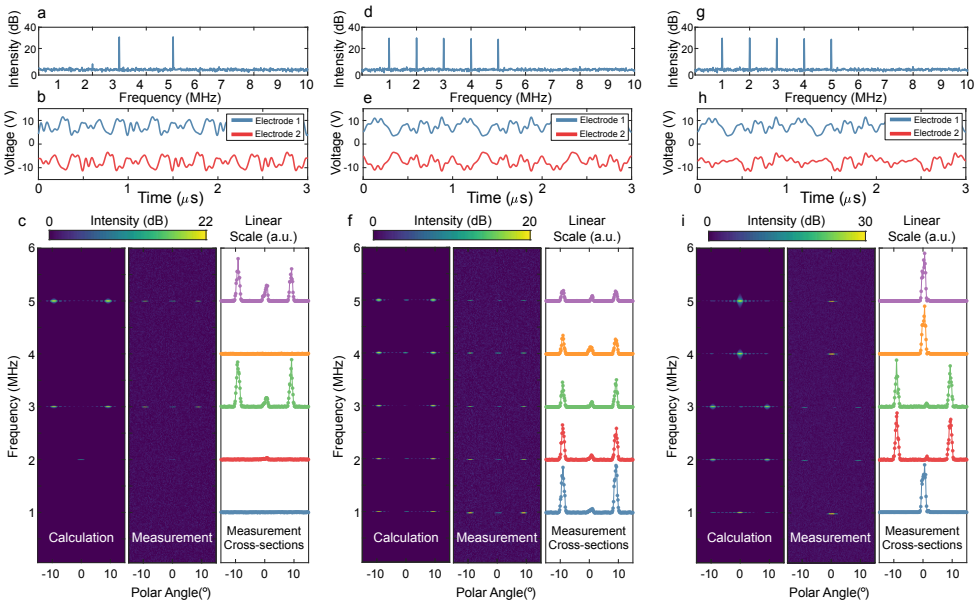

Figure 5.9: Space-time modulation for arbitrary control over the spectral and spatial properties of light. (a)–(c) Target functionality: Generate 3rd and 5th harmonics with equal amplitude, and diffract 3rd and 5th harmonics. (d)–(f) Target functionality: Generate 1st through 5th harmonics with equal amplitude, and diffract 1st through 5th harmonics. (g)–(i) Target functionality: Generate 1st through 5th harmonics, diffract 2nd and 3rd harmonics. (a),(d),(g) Measured frequency spectra after optimizing driving waveform for each target functionality of interest. (b),(e),(h) Driving voltage waveforms applied to each metasurface electrode used to generate space-time diffraction of frequencies of interest. The blue curve is applied to the entire metasurface in phase to generate frequency spectra in (a),(d),(g). (c),(f),(i) Calculated (left) and measured (center) intensity in frequency and space when the metasurface is driven with the two waveforms in (b),(e),(h), plotted in log scale. Right plots: Linear scale spatial cross-sections of measured intensity (center) at each harmonic. Note: For (g) and (h), cross-sections are normalized to the maximum intensity across all frequencies. For (i), cross-sections are normalized to the maximum intensity at each frequency.

in Fig. 5.9h. The results of space-time diffraction using these two waveforms are shown in Fig. 5.9i. As desired, the 2nd and 3rd harmonics are diffracted while the 1st, 4th and 5th are reflected normally. It should be noted that the number of frequencies generated and the spatial control over these harmonics will ultimately be limited by the time resolution or bandwidth of the waveform generator.

Sources of measured non-idealities

Throughout our space-time modulation measurements, we repeatably have signal at 0° (0th spatial order) at each diffracted frequency. In most cases, the power sent

to the 0^{th} order is much less than the $\pm$ 1^{st} orders at a given frequency, but in this section, we investigate the cause of this unwanted signal.

Any modulated intensity at the 0^{th} spatial order is a result of the total reflectance from the metasurface (i.e. average reflectance across the entire metasurface area) changing in time. Because the optimized waveforms applied to our metasurface are not symmetric about a given voltage, we would expect the time-dependent reflected field profile to also not be symmetric. If this is the case, when we time-delay a waveform, we expect the average of the reflectance for each waveform to change in time and produce a modulated signal at the 0^{th} spatial order. Figure 5.10 below explores this further.

Figure 5.10a plots the time-varying reflectance for each metasurface electrode when the metasurface is driven in the configuration shown in Fig. 5.8b. The average reflectance at each point in time, using the data from Fig 5.10a, is plotted in Fig. 5.10b and confirms that the average reflectance is in fact changing in time. Figure 5.10c plots the magnitude squared of the Fourier transform of the average time-varying amplitude (square root of the signal in Fig. 5.10b) to show the expected frequency spectrum at the 0^{th} spatial order in this driving scheme. Comparing this result to the measured data from Fig. 5.8c, the signal at 2 MHz is present, but the measured 1 MHz signal at the 0^{th} spatial order is still not accounted for.

To explain the 1 MHz signal at the 0^{th} spatial order, we hypothesized that this was caused by a slightly different reflectance response between the two electrodes of our metasurface. This could be caused by an inhomogeneous distribution of trapped charges in our dielectric, resulting in different band offsets between each electrode group. If this was the case, the average metasurface reflectance would be different than Fig. 5.10b and may contain a non-zero 1 MHz signal. To verify this idea, we assumed that one electrode had its reflectance modulation depth decreased by 10%. This case is shown in Fig. 5.10d where we again assume the same driving waveform as Fig. 5.10a but decreased the modulation depth of electrode 1 by 10%. Figure S6e plots the average reflectance from the metasurface and Fig. 5.10f plots the expected frequency response at the 0^{th} spatial order (magnitude squared of the Fourier transform of the square root of Fig. 5.10e). As expected, when the two electrodes of the metasurface do not modulate exactly the same, we see some 1 MHz signal at the 0^{th} spatial order. Unlike our measurement, the power at 1 MHz in Fig. 5.10f is less than the power at 2 MHz. However, the assumed 10% decrease in reflectance modulation is fairly small and if the difference in the response of the

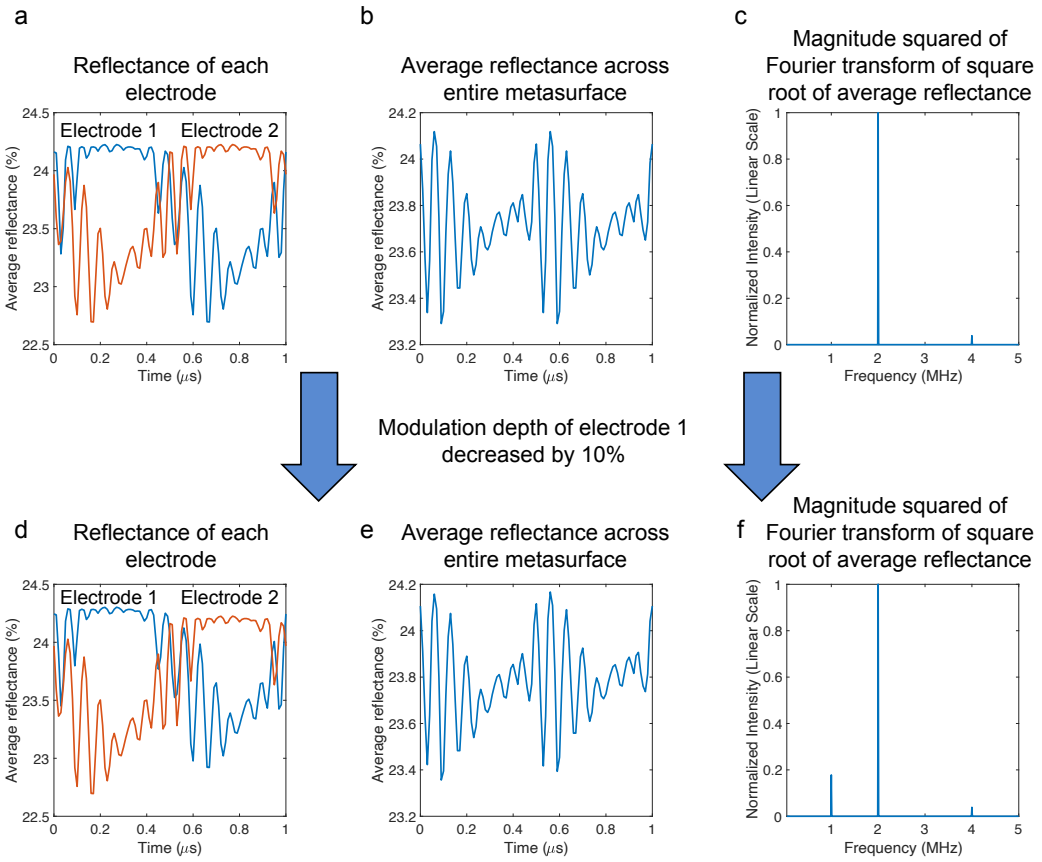

Figure 5.10: Investigation of average reflectance modulation from metasurface. For all data presented here, the optimized waveform shown in Fig. 5.5c is used, offset by half a period between each electrode. (a) Reflectance of each electrode across the metasurface over one period. (b) Average reflectance of each electrode from (a) at each point in time. (c) Magnitude squared of one-sided Fourier transform of square root of (b). (d) Reflectance of each electrode across the metasurface. The modulation depth of electrode 1 is decreased by 10%. (e) Average reflectance of each electrode from (d) at each point in time. (f) Magnitude squared of one-sided Fourier transform of square root of (e).

electrodes is larger in experiment, we would expect to see a much larger signal at 1 MHz in the 0^{th} spatial order.

If one wanted to decrease the 0^{th} spatial order signal at modulated frequencies, the optimization algorithm used to obtain the time-varying waveform could be generalized to optimize for the driving waveform for each electrode independently. By doing this, we could account for any difference in response between the two metasurface electrodes. However, for this demonstration, we were still able to demonstrate good directivity of diffraction at each frequency of interest and did not believe that this optimization was within the scope of this work.

5.9 Total efficiency of space-time diffraction

At the operating wavelength in this work (λ = 1530 nm), our devices have a reflectance of ~24% at 0 V bias. However, at this wavelength, the amplitude and phase modulation depth are relatively small and thus the overall diffraction efficiency will be limited. During "quasi-static" (purely spatial) diffraction, this means that a significant amount of power will be sent to the 0^{th} spatial order instead of the diffraction orders. Analogously, in purely time-modulation, the majority of light will be unmodulated and remain in the 0^{th} harmonic. However, for the space-time measurements in this work, we use a photodiode and spectrum analyzer to capture only the modulated frequencies reflected from our metasurface and, thus, we do not detect the strong 0^{th} harmonic signal. Because of this capability, we are able to study our space-time metasurfaces with excellent signal-to-noise ratio (SNR) without being limited by modulation depth. In this section, we account for the strong 0^{th} harmonic signal to analyze the total diffraction efficiency achieved during space-time modulated diffraction.

Figure 5.11a shows a Fourier plane camera image of the light reflected from our metasurface during space-time modulation. The metasurface modulation setup is identical to the situation portrayed in Fig. 5.8b. Because our camera captures all frequencies at once (including the unmodulated 0^{th} harmonic), we see that the image is dominated by light at the 0^{th} spatial order, which corresponds to the 0^{th} harmonic light.

From this image, it is impossible to distinguish the diffracted orders from the 0^{th} order. Figure 5.11b shows the light reflected from our metasurface when all elements are held at an identical, constant voltage. The pixel-by-pixel subtraction of Fig. 5.11b from Fig. 5.11a is plotted in Fig. 5.11c and re-normalized in Fig. 5.11d for ease of visualization. We can now clearly see the diffraction orders created by our space-time modulation, indicated by the red circles. Figure 5.11e shows an unsaturated image of light reflected from the unmodulated metasurface. (This is Fig. 5.11b with a 1000x shorter exposure time.) In order to find the total diffraction efficiency from our space-time metasurface, we used the following definition:

$$\eta = \frac{P_{-1} + P_{+1}}{P_{-1} + P_{+1} + P_0} \times \bar{R} \tag{5.1}$$

where η is diffraction efficiency, $P_{-1,0,+1}$ refer to the power (integrated intensity) in the -1^{st}, 0^{th} and $+1^{\text{st}}$ diffraction orders, respectively, and $\bar{R}$ is the average total

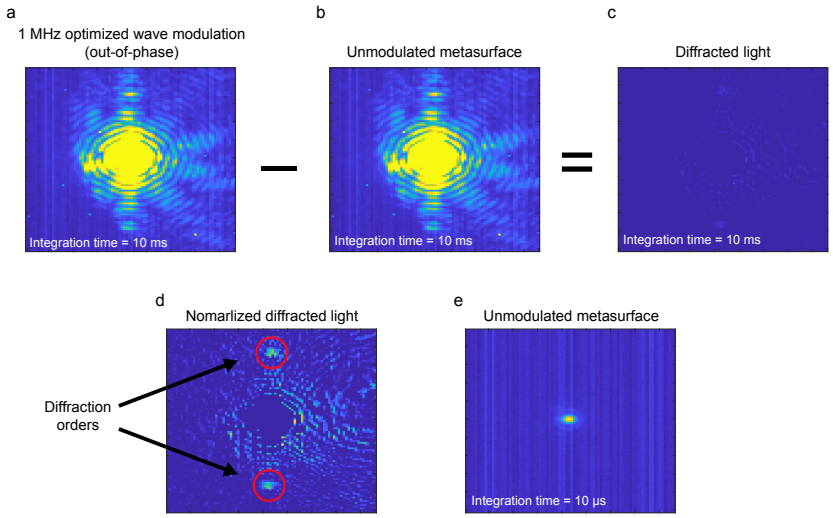

Figure 5.11: Total efficiency of space-time diffraction. Note: All sub-figures are images taken with a conventional camera placed in the Fourier plane of our imaging setup. (a) Saturated camera image of light reflected from metasurface while modulating with the optimized voltage waveform shown in Fig. 5.5c. The waveform is offset by half a period between each metasurface electrode, thus recreating the case shown in Fig. 5.8b. (b) Saturated camera image of light reflected from metasurface with equal voltage applied across the metasurface and no temporal modulation. (c) Pixel-by-pixel subtraction of (b) from (a). (d) Data from (c), normalized by the maximum intensity in (c). (e) Camera image of light reflected from metasurface without any modulation, with exposure time decreased to prevent saturation. This is (b) with 1000x smaller integration time.

reflectance. This was calculated by summing the pixel counts in the two diffracted orders in Fig. 5.11c, dividing by the pixel count in the 0^{th} order of Fig. 5.11e, dividing by 1000 (to account for the difference in exposure time), then multiplying by the average reflectance across the metasurface ~23.5%. This calculation provides a total diffraction efficiency of ~0.0036%.

By performing a similar calculation on the data plotted in Fig. 5.6f, we can compare this experimentally approximated efficiency to the expected efficiency of diffraction. (Note: in this case, we summed the intensity from diffraction in the $\pm$ 1^{st} diffraction orders for both the +1 MHz and –1 MHz signals.) This calculation provides a total efficiency of ~0.0017%, which is only roughly a factor of two different from our measured value. This agreement between measurement and calculation provides further validation to our experimental setup, device characterization, and modeling.

Our current device displays > 200° phase shift at 1470 nm, compared to the < 20° phase shift at λ = 1530 nm, the operation wavelength used in this work. One could

increase the frequency conversion efficiency at each harmonic by operating at λ = 1470 nm. However, due to instrumentation limitations, we were unable to access the wavelength of maximum phase shift using our erbium-doped fiber amplifier (which is limited to operation in the c-band) in our space-time modulation measurements. Further calculations are shown below to illustrate the improvements in efficiency that could be enabled by making use of the greater phase shift at λ = 1470 nm.

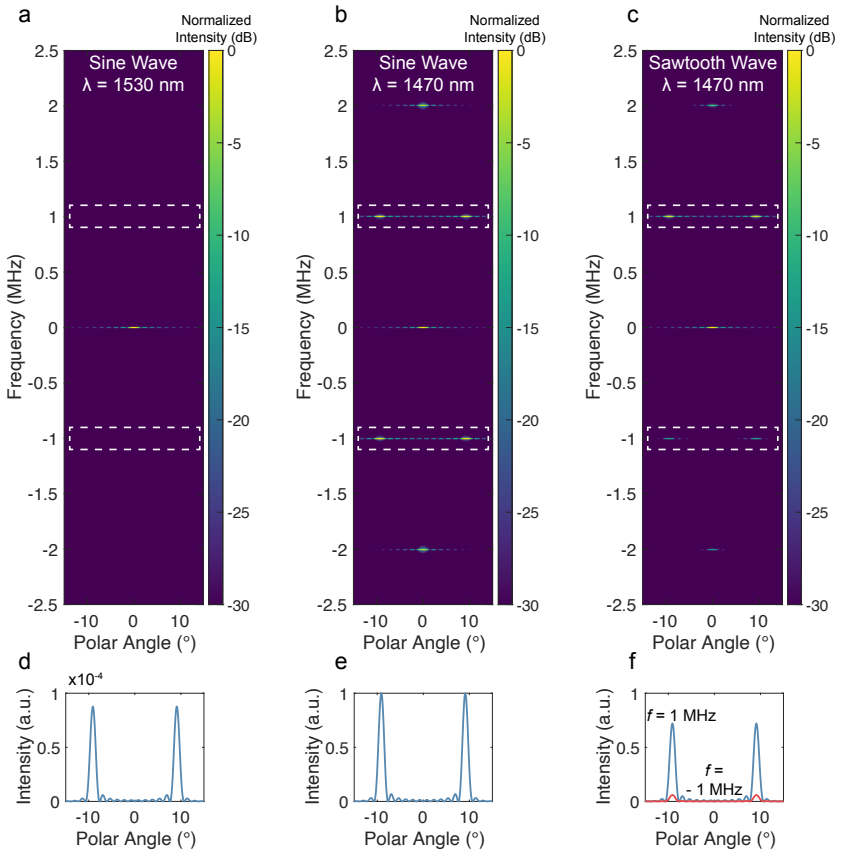

Figure 5.12: Effect of phase shift on spatiotemporal diffraction efficiency. (a) Calculated far-field intensity when modulating our device at λ = 1530 nm with two 12 V_{p-p} sine waves, offset by half a period. (b)–(c) Calculated far-field intensity when modulating our current device at λ = 1470 nm with two 12 V_{p-p} sine (b) and sawtooth (c) waveforms, offset by half a period. (a)–(c) are plotted in log scale with identical bounds, normalized to the maximum intensity across all angles and frequencies. (d)–(f) Linear spatial cross-sections taken at $f = \pm 1$ MHz, as shown by dotted white boxes in (a)–(c). The amplitude and phase values as a function of voltage at each operating wavelength were taken from measured values.

As shown in Fig. 5.12, by operating our devices at a wavelength of λ = 1470 nm, higher conversion efficiency to the generated harmonics is enabled. Figs. 5.12a–b use identical time-varying driving voltage waveforms, but the available

phase shift at λ = 1470 nm results in a larger ratio of modulated to unmodulated light. Additionally, the greater phase shift enables the generation of only positive frequencies when applying an asymmetric waveform (Fig. 5.12c). By summing the intensities in the diffracted orders at ± 1 MHz, dividing by the total intensity at all angles and frequencies, and multiplying by the average reflectance, we can obtain the total space-time diffraction efficiencies for each case illustrated above. Note: The average reflectance at λ = 1530 nm is ~23.5% whereas it is ~5% at λ = 1470 nm. The calculated diffraction efficiencies were 0.0076% for sine wave modulation at λ = 1530 nm with only amplitude modulation, 1.86% for sine wave modulation at λ = 1470 nm with > 200° phase shift, and 1.53% for sawtooth modulation at λ = 1470 nm with > 200° phase shift. Thus, by operating our current devices at a wavelength with greater phase shift, one would be able to increase the spatiotemporal diffraction efficiency by a factor of ~245.

Quasi-static performance of active metasurface

It is useful to compare the total diffraction efficiency of our metasurface during space-time modulation to the maximum achievable diffraction efficiency in the quasi-static regime. We have already presented the measured and calculated diffraction efficiency of our space-time metasurface. In the case of quasi-static diffraction, we will assume that one electrode is held at –4 V and the other at +4 V to achieve the maximum reflectance contrast possible of 22.6% and 24.2% (see Fig. 5.2f). Using these reflectance values, we performed a discrete array factor calculation to calculate the far-field intensity under this condition (Fig. 5.13). Using the definition

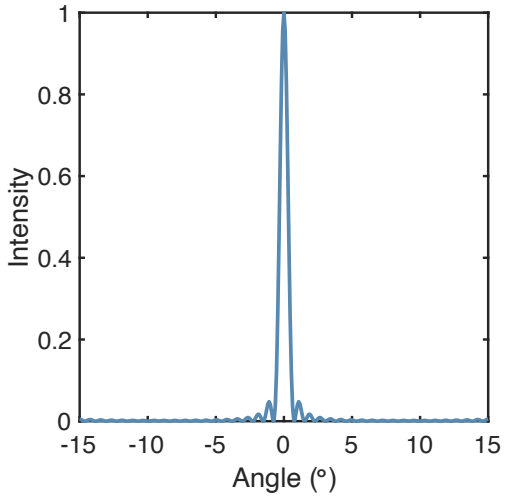

Figure 5.13: Calculated field profile during quasi-static diffraction.

provided in Equation 5.1, we obtained a total efficiency of 0.14%. As expected, this efficiency is larger (~39x) than the measured spatiotemporal diffraction efficiency. This is because during quasi-static operation, the metasurface is fixed at the largest possible amplitude contrast between the two electrodes. However, during space-time modulation, the amplitude changes over time and there will always be equal or less contrast at any given point in time than the quasi-static case, resulting in less diffracted power when integrated over time.

While space-time modulation did not improve the total diffraction efficiency compared to the quasi-static case, its ability to separate the diffracted light in frequency from "non-diffracted" light greatly improves the SNR of diffraction at the frequency of interest. This could be useful in applications if one can install bandpass filters on the detectors of interest to only select for the desired generated frequencies.

Pathways towards improved efficiency

The active metasurface community continues to develop devices with higher efficiency, larger phase shift, fast response time, and high spatial resolution of tunability. Improvements in all these of parameters will be key enablers for more efficient space-time modulation.

Regarding the transparent conducting oxide (TCO)-based plasmonic platform that we use in this work: TCO metasurfaces provide many benefits such as large phase shift, ease of electrical modulation with high spatial resolution, and fast modulation speed. However, high absorption losses in the gold and ITO makes it a poor candidate for achieving high efficiency in the long run [32]. Lately, research efforts across the active metasurface community have focused on exploring alternative active modulation schemes using lower loss materials for active permittivity modulation such as phase-change materials, electro-optic materials, and liquid crystals. We will discuss the latest advances for each technology and the limiting factors that currently prevent them from demonstrating efficient space-time modulation in the near-IR. While improvements can be made by utilizing greater phase shift, we are still fundamentally limited by the low reflectance of plasmonic metasurfaces. To improve the total reflectance or transmittance of space-time modulation, novel active metasurface designs are required.

Phase change materials: Active metasurfaces using phase-change materials make use of a large change in the real and imaginary part of refractive index when the material amorphizes or crystallizes into a different phase. While this can provide

large optical modulation, the materials require quick heating and cooling to achieve their phase transition which is commonly achieved through Joule heating or pumping with high power lasers. While it is possible to modulate these materials with fs pulsed lasers [33], electrical modulation of phase change material metasurfaces has been limited to 10s of kHz frequencies [34, 35]. For use in space-time metasurfaces, modulation frequencies should exceed the linewidth of the incident laser (typically 10s to 100s of kHz). Additionally, due to thermal crosstalk, it can be difficult to achieve the spatial resolution required for a switchable diffraction functionality [36]. With further thermal engineering, these devices may be a suitable platform for space-time modulation, but they are currently limited by slow response time and crosstalk between neighbouring elements.

Electro-optic materials: Electro-optic materials offer a promising future for active metasurfaces due to their low loss and fast speeds of electrical modulation [37]. In recent years, lithium niobate (LN) has emerged as a leading electro-optic material in the photonics community and thin film LN has become commercially available, greatly increasing the accessibility of LN-based devices. Organic electro-optic chromophores have also recently been used to demonstrate GHz amplitude modulation [37]. However, to date, electro-optic designs exhibiting tunable phase shift at subwavelength resolutions while maintaining high optical efficiencies have been shown in theory, but have not been realized experimentally [38, 39]. Klopfer et al. demonstrated a theoretical metasurface design using high Q-factor resonances with LN to achieve > 80% diffraction efficiency in simulation [38]. By using the simulated phase and amplitude values provided in this work, we calculated a total space-time diffraction efficiency of ~92% by modulating with two waveforms with an amplitude of ±10 V inverse-designed to provide a linearly phase gradient in time. This illustrates that our method presented can be used to obtain high efficiency frequency conversion if a suitable device is available. Thus, electro-optic materials are a promising platform, but tunable phase shift and beam steering have yet to be experimentally realized.

Liquid crystals: Another technique that has shown promise for high efficiency active metasurfaces is the actuation of liquid crystals (LCs), coupled to nano-resonators. While these devices have shown ~360° phase shift while maintaining > 80% reflectance in simulation [40], modulation speeds have been limited to a few kHz due to the slow relaxation time of LCs [40, 41]. While techniques are being explored to increase the speed of modulation such as thinning the LC layer and

removing alignment layers [42], there is no clear pathway to achieving significantly faster modulation frequencies beyond 10s of kHz.

While there are many exciting emerging technologies that offer the potential to enable active metasurfaces with large phase modulation, high spatial resolution, fast modulation, and high efficiency, this is still an active field of research and we believe that ITO-based plasmonic metasurfaces are an ideal testbed to explore dynamic wavefront shaping at a deeply subwavelength scale, despite their low reflectivity.

5.10 Waveform optimization algorithm

For our experimental waveform optimizations, we used the open-source genetic algorithm library in python, PyGAD. Each optimization starts by modeling the driving voltage waveform as a 20-term Fourier series with 1 MHz as the fundamental harmonic. The amplitude and phase of each harmonic term are used as inputs (or genes) to be fitted by the genetic algorithm, using random values between –1 and 1 as initial values. For each algorithm iteration, a new driving waveform was sent to the metasurface, and the reflected frequency spectrum was saved. The power at each integer harmonic frequency of 1 MHz up to 10 MHz was saved to be used for calculation of the figure-of-merit (FOM), which was maximized by the genetic algorithm over multiple generations. The genetic algorithm optimization parameters used were:

Number of generations = 80
Number of parents mating = 8
Solutions per population = 40
Number of genes = 40
Initial range low = –1
Initial range high = 1
Parent selection type = rank
Number of parents to keep = 4
Random mutation minimum value = –1
Random mutation maximum value = 1
Crossover type = single point
Mutation type = random
Mutation percent genes = 20
Elitism = 2

Frequency Spectrum	Frequency Spectrum
Maximize 1st harmonic while suppressing all others (Fig. 5.5 and 5.8)	$$FOM_1 = \frac{I[0]}{sum(I[1:])} \quad (5.2)$$
Maximize 3rd and 5th harmonic with equal intensities while suppressing all others (Figs. 5.9a–c)	$$rel = \frac{I[2] \times I[4]}{I[0] + I[1] + I[3] + sum(I[5:])} \quad (5.3)$$ $$av = \frac{I[2] + I[4]}{2} \quad (5.4)$$ $$FOM_2 = rel - abs(I[2] - av) - abs(I[4] - av) \quad (5.5)$$
Maximize 1st through 5th harmonics while suppressing all others (Figs. 5.9d–i)	$$t_1 = I[0] \quad (5.6)$$ $$t_2 = I[2] \quad (5.7)$$ $$d_1 = \sum_{i=0}^{4} abs(log_{10}(abs(I[i] - t_1))) \quad (5.8)$$ $$d_2 = \sum_{i=5}^{9} abs(log_{10}(abs(I[i] - t_2))) \quad (5.9)$$ $$FOM_3 = \frac{1}{d_1 + d_2} \quad (5.10)$$

Table 5.1: Genetic algorithm figures-of-merit (FOM).

These genetic algorithm parameters were kept constant for all optimizations, and the FOM was changed in order to obtain each frequency spectrum of interest. The FOMs used for each experimentally measured frequency spectrum are shown in Table 5.1.

Note: The variable, I, (representing the measured intensity), will be used in the FOM definitions below. This is a 1D array of the measured powers at integer frequencies from 1 to 10 MHz. The indexing and manipulation of this array will follow the convention used in python.
Example 1: I[0] = measured intensity at 1 MHz.
Example 2: sum(I[2:])= the sum of all intensities measured at integer frequencies from 3 MHz to 10 MHz. Additionally, t_1 is the power at 1 MHz using the optimized wave from FOM_1. It is now the target power for the first 5 harmonics. Similarly, t_2 is the power at 3 MHz using optimized wave from FOM_1. It is the floor of our measurement and the target power for the last 5 harmonics.

It should be noted that the selected FOMs are not necessarily the most efficient definitions to achieve the presented frequency spectra. They provided the desired frequency response in a reasonable number of algorithm iterations and are presented here for the reader's interest.

5.11 Outlook and conclusions

This work illustrates the unique capability of space-time metasurfaces to independently control the spatial and spectral properties of light. Such function can expand the capabilities of optical communication and sensing systems by increasing the information/channel capacity of a single active device. While this work serves as a proof-of-concept for space-time control at optical wavelengths using a two-electrode device, the space-time active metasurface concept can be extended to a metasurface with multiple individually addressable nanoantennas allowing for steering of frequency harmonics to arbitrary angles [26, 43, 44, 45]. Furthermore, by integrating multiple resonant elements in a single period to form a supercell, this platform could be extended to accept multiple input wavelengths of light which can be modulated independently in space and time, allowing for a multi-input, multi-output device [46]. The ability to independently control the spatial and spectral properties of light additionally provides a pathway toward realizing the violation of Lorentz reciprocity. Nonreciprocity is typically achieved by applying a large magnetic field which requires a bulky ferromagnet and limits possible applications. Spatiotemporal modulation, however, can achieve nonreciprocal functionality in a more compact system due to the breaking of time reversal symmetry. To observe large spatial separation of light (which is required for optical isolation), the modulation frequency should be close to the frequency of incident light. Because of this, nonreciprocal space-time metasurfaces have mostly been demonstrated in the RF

domain [13, 47, 48, 49]. Recent optical metasurfaces have demonstrated electrical modulation in the GHz regime [37] and could potentially be extended using the modulation schemes outlined in this work to yield small spatial offsets. However, novel optical designs would be required to realize larger spatial and spectral separation for functionalities such as optical isolation. In this context, optical pumping of space-time metasurfaces has been shown to be an effective technique to achieve large spatial separation [6, 18]. In conclusion, we have demonstrated experimental operation of near-IR metasurfaces electrically modulated at MHz frequencies to generate arbitrary harmonic spectra and individually diffract these frequencies in space. This result is enabled by the recent improvements in the modulation speed and degree of spatial phase gradient control that is possible in active metasurfaces at optical frequencies. We employed a two-electrode ITO-based plasmonic metasurface to first design a time-varying driving voltage signal to excite frequencies of interest and suppress unwanted frequencies. Next, each generated frequency was manipulated in space by introducing phase delays to specific frequency components of the driving waveform being applied to each electrode. The ability to generate and steer frequencies in a single chip-scale device has potential to find many applications in optical communication and sensing.

References

[1] J. Sisler†, P. Thureja†, M. Y. Grajower, R. Sokhoyan, I. Huang, and H. A. Atwater, "Electrically tunable space–time metasurfaces at optical frequencies," *Nature Nanotechnology*, vol. 19, pp. 1491–1498, 10 2024. DOI: 10.1038/s41565-024-01728-9.

[2] R. Tirole, S. Vezzoli, E. Galiffi, I. Robertson, D. Maurice, B. Tilmann, S. A. Maier, J. B. Pendry, and R. Sapienza, "Double-slit time diffraction at optical frequencies," *Nature Physics*, vol. 19, pp. 999–1002, 7 2023. DOI: 10.1038/s41567-023-01993-w.

[3] Z. Wu and A. Grbic, "Serrodyne frequency translation using time-modulated metasurfaces," *IEEE Transactions on Antennas and Propagation*, vol. 68, pp. 1599–1606, 3 2020. DOI: 10.1109/TAP.2019.2943712.

[4] L. Zhang, X. Q. Chen, S. Liu, Q. Zhang, J. Zhao, J. Y. Dai, G. D. Bai, X. Wan, Q. Cheng, G. Castaldi, V. Galdi, and T. J. Cui, "Space-time-coding digital metasurfaces," *Nature Communications*, vol. 9, 1 2018. DOI: 10.1038/s41467-018-06802-0.

[5] A. E. Cardin, S. R. Silva, S. R. Vardeny, W. J. Padilla, A. Saxena, A. J. Taylor, W. J. M. Kort-Kamp, H.-T. Chen, D. A. R. Dalvit, and A. K. Azad, "Surface-wave-assisted nonreciprocity in spatio-temporally modulated metasurfaces," *Nature Communications*, vol. 11, p. 1469, 1 2020. DOI: 10.1038/s41467-020-15273-1.

[6] X. Guo, Y. Ding, Y. Duan, and X. Ni, "Nonreciprocal metasurface with space–time phase modulation," *Light: Science & Applications*, vol. 8, p. 123, 1 2019. DOI: 10.1038/s41377-019-0225-z.

[7] A. Shaltout, A. Kildishev, and V. Shalaev, "Time-varying metasurfaces and lorentz non-reciprocity," *Optical Materials Express*, vol. 5, p. 2459, 11 2015. DOI: 10.1364/ome.5.002459.

[8] Y. Hadad, D. L. Sounas, and A. Alu, "Space-time gradient metasurfaces," *Physical Review B - Condensed Matter and Materials Physics*, vol. 92, 10 2015. DOI: 10.1103/PhysRevB.92.100304.

[9] S. Taravati and G. V. Eleftheriades, "Generalized space-time-periodic diffraction gratings: Theory and applications," *Physical Review Applied*, vol. 12, 2 2019. DOI: 10.1103/PhysRevApplied.12.024026.

[10] X. Wang, V. S. Asadchy, S. Fan, and S. A. Tretyakov, "Space-time metasurfaces for power combining of waves," *ACS Photonics*, vol. 8, pp. 3034–3041, 10 2021. DOI: 10.1021/acsphotonics.1c00981.

[11] M. M. Salary and H. Mosallaei, "Time-modulated conducting oxide metasurfaces for adaptive multiple access optical communication," *IEEE Transactions on Antennas and Propagation*, vol. 68, pp. 1628–1642, 3 2020. DOI: 10.1109/TAP.2019.2938613.

[12] R. Sabri, M. M. Salary, and H. Mosallaei, "Quasi-static and time-modulated optical phased arrays: Beamforming analysis and comparative study," *Advanced Photonics Research*, vol. 2, 9 2021. DOI: 10.1002/adpr.202100034.

[13] S. Taravati, N. Chamanara, and C. Caloz, "Nonreciprocal electromagnetic scattering from a periodically space-time modulated slab and application to a quasisonic isolator," *Physical Review B*, vol. 96, p. 165 144, 16 2017. DOI: 10.1103/PhysRevB.96.165144.

[14] S. Taravati, "Aperiodic space-time modulation for pure frequency mixing," *Physical Review B*, vol. 97, p. 115 131, 11 2018. DOI: 10.1103/PhysRevB.97.115131.

[15] P. K. Tien, "Parametric amplification and frequency mixing in propagating circuits," *Journal of Applied Physics*, vol. 29, pp. 1347–1357, 9 1958. DOI: 10.1063/1.1723440.

[16] L. Zhang and T. J. Cui, "Space-time-coding digital metasurfaces: Principles and applications," *Research*, vol. 2021, 2021. DOI: 10.34133/2021/9802673.

[17] L. Zhang, X. Q. Chen, R. W. Shao, J. Y. Dai, Q. Cheng, G. Castaldi, V. Galdi, and T. J. Cui, "Breaking reciprocity with space-time-coding digital metasurfaces," *Advanced Materials*, vol. 31, 41 2019. DOI: 10.1002/adma.201904069.

[18] M. Karimi, M. Z. Alam, J. Upham, O. Reshef, and R. W. Boyd, "Time-varying gradient metasurface with applications in all-optical beam steering," *Nanophotonics*, vol. 12, pp. 1733–1740, 9 2023. DOI: 10.1515/nanoph-2022-0756.

[19] E. Lustig, O. Segal, S. Saha, E. Bordo, S. N. Chowdhury, Y. Sharabi, A. Fleischer, A. Boltasseva, O. Cohen, V. M. Shalaev, and M. Segev, "Time-refraction optics with single cycle modulation," *Nanophotonics*, vol. 12, pp. 2221–2230, 12 2023. DOI: 10.1515/nanoph-2023-0126.

[20] X. Song, W. Yang, K. Qu, X. Bai, K. Chen, Y. Feng, and W. Zhu, "Switchable metasurface for nearly perfect reflection, transmission, and absorption using PIN diodes," *Optics Express*, vol. 29, p. 29 320, 18 2021. DOI: 10.1364/oe.436261.

[21] S. Ahadi, M. Neshat, and M. K. Moravvej-Farshi, "Binary THz modulator based on silicon Schottky-metasurface," *Scientific Reports*, vol. 12, p. 18 871, 1 2022. DOI: 10.1038/s41598-022-23534-w.

[22] C. Huang, B. Sun, W. Pan, J. Cui, X. Wu, and X. Luo, "Dynamical beam manipulation based on 2-bit digitally-controlled coding metasurface," *Scientific Reports*, vol. 7, p. 42 302, 1 2017. DOI: 10.1038/srep42302.

[23] P. Thureja, G. K. Shirmanesh, K. T. Fountaine, R. Sokhoyan, M. Grajower, and H. A. Atwater, "Array-level inverse design of beam steering active metasurfaces," *ACS Nano*, vol. 14, pp. 15 042–15 055, 11 2020. DOI: 10.1021/acsnano.0c05026.

[24] M. M. Salary, S. Farazi, and H. Mosallaei, "A dynamically modulated all-dielectric metasurface doublet for directional harmonic generation and manipulation in transmission," *Advanced Optical Materials*, vol. 7, 23 2019. DOI: 10.1002/adom.201900843.

[25] Y.-W. Huang, H. W. H. Lee, R. Sokhoyan, R. A. Pala, K. Thyagarajan, S. Han, D. P. Tsai, and H. A. Atwater, "Gate-tunable conducting oxide metasurfaces," *Nano Letters*, vol. 16, pp. 5319–5325, 9 2016. DOI: 10.1021/acs.nanolett.6b00555.

[26] G. K. Shirmanesh, R. Sokhoyan, P. C. Wu, and H. A. Atwater, "Electro-optically tunable multifunctional metasurfaces," *ACS Nano*, vol. 14, pp. 6912–6920, 6 2020. DOI: 10.1021/acsnano.0c01269.

[27] G. K. Shirmanesh, R. Sokhoyan, R. A. Pala, and H. A. Atwater, "Dual-gated active metasurface at 1550 nm with wide (>300°) phase tunability," *Nano Letters*, vol. 18, pp. 2957–2963, 5 2018. DOI: 10.1021/acs.nanolett.8b00351.

[28] R. Amin, R. Maiti, Y. Gui, C. Suer, M. Miscuglio, E. Heidari, J. B. Khurgin, R. T. Chen, H. Dalir, and V. J. Sorger, "Heterogeneously integrated ITO plasmonic Mach–Zehnder interferometric modulator on SOI," *Scientific Reports*, vol. 11, 1 2021. DOI: 10.1038/s41598-020-80381-3.

[29] B. Lu, H. Lv, Y. Zhang, Y. Zhang, and C. Liu, "Comparison of HfAlO, Hfo_2/Al_2O_3, and HfO_2 on n-type GaAs using atomic layer deposition," *Superlattices and Microstructures*, vol. 99, pp. 54–57, 2016. DOI: 10.1016/j.spmi.2016.07.032.

[30] Y. Gui, B. M. Nouri, M. Miscuglio, R. Amin, H. Wang, J. B. Khurgin, H. Dalir, and V. J. Sorger, "100 GHz micrometer-compact broadband monolithic ITO Mach–Zehnder interferometer modulator enabling 3500 times higher packing density," *Nanophotonics*, vol. 11, pp. 4001–4009, 17 2022. DOI: 10.1515/nanoph-2021-0796.

[31] R. Amin, R. Maiti, Y. Gui, C. Suer, M. Miscuglio, E. Heidari, R. T. Chen, H. Dalir, and V. J. Sorger, "Sub-wavelength GHz-fast broadband ITO Mach–Zehnder modulator on silicon photonics," *Optica*, vol. 7, p. 333, 4 2020. DOI: 10.1364/OPTICA.389437.

[32] R. Sokhoyan, P. Thureja, J. Sisler, M. Grajower, K. Shayegan, E. Feigenbaum, S. Elhadj, and H. A. Atwater, "Electrically tunable conducting oxide metasurfaces for high power applications," *Nanophotonics*, vol. 12, pp. 239–253, 2 2023. DOI: 10.1515/nanoph-2022-0594.

[33] A.-K. U. Michel, P. Zalden, D. N. Chigrin, M. Wuttig, A. M. Lindenberg, and T. Taubner, "Reversible optical switching of infrared antenna resonances with ultrathin phase-change layers using femtosecond laser pulses," *ACS Photonics*, vol. 1, pp. 833–839, 9 2014. DOI: 10.1021/ph500121d.

[34] S. Abdollahramezani, O. Hemmatyar, M. Taghinejad, H. Taghinejad, A. Krasnok, A. A. Eftekhar, C. Teichrib, S. Deshmukh, M. A. El-Sayed, E. Pop, M. Wuttig, A. Alù, W. Cai, and A. Adibi, "Electrically driven reprogrammable phase-change metasurface reaching 80% efficiency," *Nature Communications*, vol. 13, p. 1696, 1 2022. DOI: 10.1038/s41467-022-29374-6.

[35] Y. Wang, P. Landreman, D. Schoen, K. Okabe, A. Marshall, U. Celano, H.-S. P. Wong, J. Park, and M. L. Brongersma, "Electrical tuning of phase-change antennas and metasurfaces," *Nature Nanotechnology*, vol. 16, pp. 667–672, 6 2021. DOI: 10.1038/s41565-021-00882-8.

[36] Y. Zhang, C. Fowler, J. Liang, B. Azhar, M. Y. Shalaginov, S. Deckoff-Jones, S. An, J. B. Chou, C. M. Roberts, V. Liberman, M. Kang, C. Ríos, K. A. Richardson, C. Rivero-Baleine, T. Gu, H. Zhang, and J. Hu, "Electrically reconfigurable non-volatile metasurface using low-loss optical phase-change material," *Nature Nanotechnology*, vol. 16, pp. 661–666, 6 2021. DOI: 10.1038/s41565-021-00881-9.

[37] I.-C. Benea-Chelmus, S. Mason, M. L. Meretska, D. L. Elder, D. Kazakov, A. Shams-Ansari, L. R. Dalton, and F. Capasso, "Gigahertz free-space electro-optic modulators based on Mie resonances," *Nature Communications*, vol. 13, p. 3170, 1 2022. DOI: 10.1038/s41467-022-30451-z.

[38] E. Klopfer, S. Dagli, D. Barton, M. Lawrence, and J. A. Dionne, "High-quality-factor silicon-on-lithium niobate metasurfaces for electro-optically reconfigurable wavefront shaping," *Nano Letters*, vol. 22, pp. 1703–1709, 4 2022. DOI: 10.1021/acs.nanolett.1c04723.

[39] A. Weiss, C. Frydendahl, J. Bar-David, R. Zektzer, E. Edrei, J. Engelberg, N. Mazurski, B. Desiatov, and U. Levy, "Tunable metasurface using thin-film lithium niobate in the telecom regime," *ACS Photonics*, vol. 9, pp. 605–612, 2 2022. DOI: 10.1021/acsphotonics.1c01582.

[40] P. Moitra, X. Xu, R. M. Veetil, X. Liang, T. W. W. Mass, A. I. Kuznetsov, and R. Paniagua-Domínguez, "Electrically tunable reflective metasurfaces with continuous and full-phase modulation for high-efficiency wavefront control at visible frequencies," *ACS Nano*, vol. 17, pp. 16 952–16 959, 17 2023. DOI: 10.1021/acsnano.3c04071.

[41] M. A. Aisheh, M. Abutoama, M. J. Abuleil, and I. Abdulhalim, "Fast tunable metamaterial liquid crystal achromatic waveplate," *Nanophotonics*, vol. 12, pp. 1115–1127, 6 2023. DOI: 10.1515/nanoph-2022-0656.

[42] R. M. Veetil, X. Xu, J. Dontabhaktuni, X. Liang, A. I. Kuznetsov, and R. Paniagua-Dominguez, "Nanoantenna induced liquid crystal alignment for high performance tunable metasurface," *Nanophotonics*, vol. 0, 0 2023. DOI: 10.1515/nanoph-2023-0446.

[43] R. Sabri, M. M. Salary, and H. Mosallaei, "Broadband continuous beam-steering with time-modulated metasurfaces in the near-infrared spectral regime," *APL Photonics*, vol. 6, 8 2021. DOI: 10.1063/5.0051815.

[44] G. Castaldi, L. Zhang, M. Moccia, A. Y. Hathaway, W. X. Tang, T. J. Cui, and V. Galdi, "Joint multi-frequency beam shaping and steering via space–time-coding digital metasurfaces," *Advanced Functional Materials*, vol. 31, 6 2021. DOI: 10.1002/adfm.202007620.

[45] B. H.-X. Xu, J. Xu, Y. Wang, C. Wang, F. Zhang, and G. Hu, "Multi-channel metasurfaces with frequency-direction multiplexed amplitude and phase modulations," *Advanced Optical Materials*, vol. 11, 22 2023. DOI: 10.1002/adom.202301299.

[46] R. Sabri, A. Forouzmand, and H. Mosallaei, "Multi-wavelength voltage-coded metasurface based on indium tin oxide: Independently and dynamically controllable near-infrared multi-channels," *Optics Express*, vol. 28, p. 3464, 3 2020. DOI: 10.1364/OE.382926.

[47] S. Taravati and G. V. Eleftheriades, "Microwave space-time-modulated metasurfaces," *ACS Photonics*, vol. 9, pp. 305–318, 2 2022. DOI: 10.1021/acsphotonics.1c01041.

[48] Y. Hadad, J. C. Soric, and A. Alu, "Breaking temporal symmetries for emission and absorption," *Proceedings of the National Academy of Sciences*, vol. 113, pp. 3471–3475, 13 2016. DOI: 10.1073/pnas.1517363113.

[49] S. Taravati and G. V. Eleftheriades, "Full-duplex nonreciprocal beam steering by time-modulated phase-gradient metasurfaces," *Physical Review Applied*, vol. 14, p. 014 027, 1 2020. DOI: 10.1103/PhysRevApplied.14.014027.

Chapter 6

A MILLIMETER-SCALE OPTICALLY ADDRESSABLE ACTIVE TRANSMISSIVE METASURFACE USING LIQUID CRYSTAL REORIENTATION

The material in this chapter was in part presented in

J. Sisler, C. U. Hail, Z. S. Davidson, J. Gao, A. Fehr, R. Sokhoyan, S. Elhadj, and H. A. Atwater, "An optically addressable transmissive liquid crystal metasurface spatial light modulator," 2026. arXiv: 2603.20574 [physics.optics]. [Online]. Available: https://arxiv.org/abs/2603.20574

[This chapter is temporarily embargoed.]

Chapter 7

SUMMARY AND OUTLOOK

In this thesis, we described the design and characterization of active metasurfaces using two distinct active materials: indium tin oxide (ITO) and liquid crystals (LCs). For both systems, a detailed understanding of the material was required to make a fully functioning device. While both ITO and LCs are very mature materials used in a wide range of consumer electronics, they still require extensive engineering when used in applications/materials environments which are different than their typical use cases. The work presented in this thesis has focused on proof-of-principle demonstrations of new optical designs, modulation motifs, and materials processing. However, from the knowledge gained from each project, there are many interesting new directions that could be explored in the future. We will now summarize each chapter and outline some of our proposed possible future research directions.

In Chapter 1, we present an introduction to metasurfaces (both passive and active), describing the theory behind their operation and some notable examples. We focus our discussion on the design of active metasurfaces and how they can be used in different operation modes, which remains the focus of the rest of the thesis.

Chapter 2 provides a detailed description of ITO and how its properties can be manipulated for the design and fabrication of advanced active metasurface devices. The information presented in this section represents years of process development and characterization of ITO films when annealed in different material environments. We find that the carrier concentration and epsilon-near-zero (ENZ) wavelength of an ITO film can be significantly tuned through low temperature (150 °C) anneals in air or vacuum. Annealing in air (vacuum) decreases (increases) carrier concentration and red (blue) shifts the ENZ wavelength. Despite the great amount of post-fabrication tunability that is possible with ITO films, it is very difficult to maintain desired properties when ITO is integrated into a complex stack of materials required for a working electro-optic device. For example, atomic layer deposition (ALD) growth of oxides on top of a film of ITO will greatly increase the ITO carrier concentration. While oxides deposited on ITO films at room temperature via electron beam evaporation do not significantly change the ITO immediately after deposition, the full stack will be extremely temperature sensitive due to the high concentration

of oxygen vacancies in the evaporated oxide film. Thus, any small increase in temperature later in a fabrication process (even temperatures as low 50 °C) will cause an increase in the carrier concentration of the ITO film. We also outline the interaction between ITO and various other materials in this chapter. The conclusions and methods presented here will be useful to anyone who needs to prepare ITO films with specific electrical or optical properties.

Future research directions should explore possible materials that can act as effective encapsulants for ITO. For example, we observed that ITO films become more temperature sensitive when they are in contact with an oxygen deficient oxide such as evaporated Al_2O_3. However, one could explore oxides that tend to be oxygen-rich (e.g. MoO_3) as well as nitrides (e.g. AlN). We briefly explored these materials as encapsulating layers on top of ITO which could potentially decrease the temperature sensitivity and observed some promising results. Future work is required to optimize the deposition such that there is minimal interaction between the encapsulating material and the ITO layer. Such a film would enable much more reliable active metasurface devices utilizing ITO as an active material, especially for devices that are designed to modulate emissivity.

In Chapter 3, we present a novel process for introducing spatially varying doping profiles within a planar film of ITO. The process involves patterning electron beam evaporated Al_2O_3 on top of a thin film of ITO, the low temperature anneal (150 °C) for a few hours, then the selective of the evaporated Al_2O_3 in the common photoresist developer, MF-319. This process allows for selective doping of regions of ITO that were originally covered by evaporated Al_2O_3. Such a device was first measured via atomic force microscope (AFM) to ensure that there were no geometric variations across the final ITO film. Then, its reflectance was measured, which exhibited clear plasmonic modes excited by the contrast in carrier concentration within the ITO layer.

The process introduced here could find application in many interesting optical devices which make use of the inherent epsilon-near-zero (ENZ) crossing of ITO films. For example, the work of Silveirinha et al. showed that an arbitrarily shaped ENZ region can be used to connect two waveguides with near-zero reflectance [1]. Thus, one could imagine using the introduced process to arbitrarily define thin ENZ regions to connect on-chip waveguides that need to make a turn with a sharp bend radius. Another possible direction is the fabrication of planar and conductive metasurfaces made by patterning the properties of ITO rather than etching the into

the ITO to create geometric variations. Such a metasurface could be useful for applications where a metasurface must be conductive such as for the trapping of charged ions. Finally, this work has only shown the binary patterning of two different carrier concentrations of ITO. To further develop this technique and to extend the possible applications, future research should explore creating a process to produce spatially varying carrier concentration gradients in a film of ITO. Such a device could be used for the creation of a plasmonic on-chip spectrometer.

Chapter 4 presents an active metasurface based upon field-effect carrier depletion in thin films of ITO to enable the tunable diffraction of mid-IR light in two dimensions (2D) as well as patternable emissivity modulation. First, we designed a unique device architecture which allows for the integration of an ITO layer with very low carrier concentration into a final active device. This is difficult to achieve because of the temperature sensitivity of ITO when in contact with various other materials. We then verified the performance of our device by demonstrating tunable diffraction of reflected coherent light in the mid-IR. Next, we altered our device architecture to allow for the tunable diffraction of mid-IR light in 2D for any input polarization state. Finally, by heating up our device, we demonstrated the reconfigurable patterning of emissivity of light in 2D.

Future work in this area could first optimize device fabrication to obtain larger phase modulation in the current device architecture. This would allow for 2D beam-steering to arbitrary angles in contrast to the diffraction in two orthogonal axes which was demonstrated here. Additionally, future design work could explore alternative designs for the tunable beam-steering of thermally emitted light, similar to the work shown by Siegel et al. [2]. The work by Siegel et al. was limited to the binary switching of thermally emitted light between two directions. However, by designing a more advanced device using principles previously demonstrated for passive structures to achieve directive thermal emission [3], [4], [5], [6], [7], [8], one could demonstrate the continuous steering of directive thermally emitted light. This would represent a great breakthrough for the field of thermal photonics.

In Chapter 5, we used a reflective gate-tunable ITO-based metasurface — similar in design to the device presented in Chapter 4 — operating at 1530 nm to generate diffraction of frequency-shifted sidebands in the MHz. Our device consists of an array of interdigitated plasmonic nanoantennas with two electrical contacts initially modulated in-phase such that harmonic sidebands generated off the incident light are normally reflected. Next, we time-delayed the electrical waveforms by half

a period such that a spatial binary phase grating was achieved. This directs the frequency-shifted light to the $\pm 1^{st}$ diffraction orders, enabling space-time switchable diffraction. Due to the nonideal properties of our metasurface (i.e. a co-varying and nonlinear amplitude and phase response), the diffraction efficiency was limited. This was increased by optimizing the driving waveform from an arbitrary waveform generator to improve the frequency conversion efficiency to any desired frequency spectra. Finally, we demonstrated the near-arbitrary generation of frequency spectra of interest, and the independent switchable diffraction of each generated frequency.

Future work related to this project could explore designs which enable multi-frequency, multi-beam steering of light. This could be enabled by integrating multiple resonant elements in a supercell configuration and independently modulating each structure with a different time-varying waveform. Additionally, by introducing more electrode connections, we could steer light to a continuous range of angles, rather than the binary switchable diffraction functionality which was demonstrated here. More generally, one could explore faster modulation of such metasurfaces using all-optical pumping schemes [9], [10], [11] to demonstrate more exotic phenomena such as time-crystals [11], [12], [13].

Finally, in Chapter 6 we present an optically addressed large area active metasurface for the polarization conversion of near-IR light ($\lambda = 1$ μm) in 2D. Our device is based on a TiO_2 metasurface submerged in a thin (~2 μm) LC layer. The top contact of our device is the photoconductor, bismuth silicon oxide (BSO), which can be used to apply a 2D patternable voltage when illuminated with a pump laser at $\lambda = 435$ nm. Thus, we imaged a pattern on our device with a blue laser, which then switched the underlying LCs such that the polarization of the probe laser at $\lambda = 1$ μm obtained the pattern of the blue laser. We demonstrated the 2D patterning of polarization across an active area of 5x5 mm^2 with an efficiency of 60%. The switching speed of our LC-metasurface device was approximately two times faster than an equivalent cell with no metasurface layer. Additionally, we studied the interactions of LCs with the TiO_2 nanostructures and found that their alignment was strongly influenced by the nanoscale geometry. By first simulating how the LCs aligned around our TiO_2 metasurface and importing the resulting spatially varying refractive index profiles into our optical simulations, we obtained an improved agreement with our measured transmittance spectra. Additionally, we simulated the spatially varying electric field throughout the device to first predict the dynamic 3D LC director fields, then the final optical transmittance. By taking a multiphysics approach to our design, we

obtained an improved model of LC-metasurfaces.

Future work on LC-metasurfaces should first explore the design of new devices exhibiting phase modulation by employing our developed model of the LC dynamics within the device. By designing optical modes with field predominantly above the metasurface pillars, more optical modulation could be enabled. Additionally, the exploration of different materials could enable improved performance. For example, dual frequency LCs tend to switch faster than conventional LCs because they can be actively driven during both switching states. Additionally, photoactive top contact materials other than BSO should be evaluated to improve the spatial resolution of the system. This will allow for higher quality patterning as well as a wider field of view during beam-steering applications. Finally, we discovered that the applied electrostatic field was very low in between the substituent TiO_2 nanostructures. This is primarily because the TiO_2 has a very large dielectric permittivity (~100) compared to the permittivity of the LCs (~6–17). Thus, by designing a metasurface with a lower DC permittivity of its constituent nanostructures, more field could be used to switch the LCs between adjacent pillars. This would allow more flexibility in the optical design and overall modulation.

References

[1] M. Silveirinha and N. Engheta, "Tunneling of electromagnetic energy through subwavelength channels and bends using epsilon-near-zero materials," *Physical Review Letters*, vol. 97, p. 157 403, 15 2006. DOI: 10.1103/PhysRevLett.97.157403.

[2] J. Siegel, S. Kim, M. Fortman, C. Wan, M. A. Kats, P. W. C. Hon, L. Sweatlock, M. S. Jang, and V. W. Brar, "Electrostatic steering of thermal emission with active metasurface control of delocalized modes," *Nature Communications*, vol. 15, p. 3376, 1 2024. DOI: 10.1038/s41467-024-47229-0.

[3] J.-J. Greffet, R. Carminati, K. Joulain, J.-P. Mulet, S. Mainguy, and Y. Chen, "Coherent emission of light by thermal sources," *Nature*, vol. 416, pp. 61–64, 6876 2002. DOI: 10.1038/416061a.

[4] T. Inoue, M. D. Zoysa, T. Asano, and S. Noda, "Realization of narrowband thermal emission with optical nanostructures," *Optica*, vol. 2, p. 27, 1 2015. DOI: 10.1364/OPTICA.2.000027.

[5] C. Arnold, F. Marquier, M. Garin, F. Pardo, S. Collin, N. Bardou, J.-L. Pelouard, and J.-J. Greffet, "Coherent thermal infrared emission by two-dimensional silicon carbide gratings," *Physical Review B*, vol. 86, p. 035 316, 3 2012. DOI: 10.1103/PhysRevB.86.035316.

[6] J. Yu, R. Qin, Y. Ying, M. Qiu, and Q. Li, "Asymmetric directional control of thermal emission," *Advanced Materials*, vol. 35, 45 2023. DOI: 10.1002/adma.202302478.

[7] J. R. Nolen, A. C. Overvig, M. Cotrufo, and A. Alù, "Local control of polarization and geometric phase in thermal metasurfaces," *Nature Nanotechnology*, vol. 19, pp. 1627–1634, 11 2024. DOI: 10.1038/s41565-024-01763-6.

[8] A. C. Overvig, S. A. Mann, and A. Alù, "Thermal metasurfaces: Complete emission control by combining local and nonlocal light-matter interactions," *Physical Review X*, vol. 11, p. 021 050, 2 2021. DOI: 10.1103/PhysRevX.11.021050.

[9] R. Tirole, S. Vezzoli, E. Galiffi, I. Robertson, D. Maurice, B. Tilmann, S. A. Maier, J. B. Pendry, and R. Sapienza, "Double-slit time diffraction at optical frequencies," *Nature Physics*, vol. 19, pp. 999–1002, 7 2023. DOI: 10.1038/s41567-023-01993-w.

[10] M. Karimi, M. Z. Alam, J. Upham, O. Reshef, and R. W. Boyd, "Time-varying gradient metasurface with applications in all-optical beam steering," *Nanophotonics*, vol. 12, pp. 1733–1740, 9 2023. DOI: 10.1515/nanoph-2022-0756.

[11] E. Lustig, O. Segal, S. Saha, E. Bordo, S. N. Chowdhury, Y. Sharabi, A. Fleischer, A. Boltasseva, O. Cohen, V. M. Shalaev, and M. Segev, "Time-refraction

optics with single cycle modulation," *Nanophotonics*, vol. 12, pp. 2221–2230, 12 2023. DOI: 10.1515/nanoph-2023-0126.

[12] X. Wang, P. Garg, M. S. Mirmoosa, A. G. Lamprianidis, C. Rockstuhl, and V. S. Asadchy, "Expanding momentum bandgaps in photonic time crystals through resonances," *Nature Photonics*, vol. 19, pp. 149–155, 2 2025. DOI: 10.1038/s41566-024-01563-3.

[13] A. Dikopoltsev, Y. Sharabi, M. Lyubarov, Y. Lumer, S. Tsesses, E. Lustig, I. Kaminer, and M. Segev, "Light emission by free electrons in photonic time-crystals," *Proceedings of the National Academy of Sciences*, vol. 119, 6 2022. DOI: 10.1073/pnas.2119705119.